Operando Imaging Techniques for Probing Local Electrochemical Response in Solids

Brian Gerwe

A dissertation

submitted in partial fulfillment of the

requirements for the degree of

Doctor of Philosophy

University of Washington

2021

Reading Committee:

Stuart Adler, Chair

Daniel Schwartz

Gerald Seidler

Program Authorized to Offer Degree:

Chemical Engineering

University of Washington

Abstract

Operando Imaging Techniques for Probing Local Electrochemical Response in Solids

Brian Gerwe

Chair of the Supervisory Committee:
Professor Stuart Adler
Chemical Engineering

Global energy supplies are transitioning to renewable sources, such as solar and wind; however, widespread adoption is contingent upon a new generation of energy conversion and storage devices, such as fuel cells and batteries. Kinetic and transport properties at the micro- and nanoscale govern these devices' performance; therefore, directly measuring them is crucial for continued development. Conventional characterization techniques–like impedance spectroscopy–must infer the microscopic behavior from an aggregate response–an average of rates over the entire sample geometry –and may be distorted by local inhomogeneities. Others have developed chemically sensitive *in situ* or *operando* techniques targeting these length scales, but these methods focus on steady-state or stepwise responses that simultaneously probe a broad range of timescales.

In this work, we introduce frequency-resolved X-ray absorption spectroscopy (FR-XAS) to probe electrode response both spatially and temporally during a global impedance perturbation.

As a model system, we studied a thin film solid oxide fuel cell cathode material ($La_{1-x}Sr_xCoO_{3-\delta}$) with a patterned insulating layer to restrict contact between the electrolyte and electrode. With FR-XAS, we captured 1-dimensional images of oxygen vacancy profiles in the patterned film, representing the first direct measurements of concentration distributions associated with a Gerischer or Warburg impedance. We successfully extracted vacancy diffusion and surface exchange rate parameters using a 1-dimensional model, independent of the impedance response, which deviated from the expected Gerischer shape. Unexpected contributions from the insulating layer explain most of the discrepancy, though the exact response mechanism is an open question.

Finally, we use strain-based atomic force microscopy methods to probe the space charge region (SCR) at grain boundaries in polycrystalline acceptor-doped ceria. We report images of ceria under DC polarization using scanning thermo-ionic microscopy–a recently developed technique that probes ionic concentration via thermal stress. The results show promising signs of manipulating the SPR; however, inconsistent responses across some grain boundaries and large topographic changes prevent unambiguous conclusions.

TABLE OF CONTENTS

LIST OF FIGURES

LIST OF TABLES

ACKNOWLEDGEMENTS

I am immensely grateful to all the people who have defined my graduate school experience over the last six year. First, I'd like to thank my committee members Stuart Adler (Chair), Dan Schwartz, and Jerry Seidler, whose feedback and enthusiasm have inspired me in this journey.

I want to extend extra appreciation to Stuart Adler for his endless patience, teachings, and guidance. I came to graduate school wanting to learn more about the core principles of Chemical Engineering and I have exceeded those expectations under his mentorship. Furthermore, he has shown tremendous trust and support by sending me on many research trips to Japan—it's hard to overstate the importance of those trips in my graduate career.

Next, I would like to thank Professor Koji Amezawa from Tohoku University in Sendai, Japan, and his incredibly talented students: Keita Mizuno, Shota Kageyama, Dr. Mahunnop Fakkao, Katsuya Nishidate, Takaaki Imaizumi, and Kota Motohashi. I am deeply appreciative or your brilliance, kind hospitality, and limitless hard work.

A big thank you to all my friends in Seattle. The bandmates: Joe DeMaria, Dr. Ed Michor, Dr. Willy Voje, Dr. Jac Clark, and Dr. Matt Crane. The coffee crew: Dr. Elena Pandres, Dr. Elisa Harrison, and Dr. Kyle Caldwell. The electrochemists: Dr. Matt Murbach, Victor Hu, Erica Eggleton, Linette Teo, and Dr. Trevor Braun. Members of my cohort: Dr. Ben Ponto, Dr. Neal Dawson-Elli, Dr. Caitlyn Wolf, Dr. Kyle Harrigan, and Dr. Jay Rutherford. The housemates: Dr. Josh Smith and Dr. Wesley Beckner. Current labmates and alumni: Dr. Tim Geary, Dr. Cortney Kreller, Dr. Honorio Valdes Espinosa de los Monteros, Dr. Jon Witt, Dr. Kelly Carpenter, Isaac Kretzmer, Giang Le, Anthony Pyka, and Maria Politi. And others I have met along the way: Sheila Goodman, Laura Dobroski, Audrey Michniak, Kailin Lu, and Ruthie Berk.

Next, thanks to my friends, colleagues, and mentors who have inspired or otherwise supported my passion for chemical engineering. My UA classmates: Phil Befus, Jerad Dunevant, Daniel Witter, Kate Li, Mike Flammia, Dr. Rachel Braun, and Dr. Cris Mariscal. My lifelong friends: Alec Latino, Ian Boelts, Wrenn Bunker-Koesters, and Seth Krieger. The UA ChEE faculty: Dr. Paul Blowers, Dr. Armin Sorooshian, Dr. Greg Ogden, and Dr. Kim Ogden. To the educators who first inspired my passion for math and chemistry, without whom I would not have embarked down this wonderful path: Mike Robinette and Dr. Janet Munro.

To my incredibly supportive current and future families: My mother, Molly, for always making sure I was taking studying hard and care of myself. My father, Jeff, who instilled in me the value and rewards of a good work ethic. My brother, Alex, for teaching me critical thinking, and always asking tough questions about my work. My future in-laws, the Blaires: Mike, Dorothy, Rachael, Jessica, and Shannon, for accepting me as a part of their family, and teaching me to love musicals and karaoke.

Finally, to my amazing, talented, and dedicated partner, Lindsay Blaire. I could not have survived graduate school without you by my side. You illuminate every moment we spend together, and I cannot wait to spend the rest of our lives together.

DEDICATION

To my present and future families, whose support sustained me.

Chapter 1. INTRODUCTION

Solid oxide fuel cells (SOFC) are electrochemical devices composed of a fuel electrode (anode), ceramic electrolyte, and an oxygen electrode (cathode) used to convert chemical energy into electrical energy efficiently. Coupling SOFCs with water electrolyzers–to convert electricity into chemical energy stored in H_2– is an attractive option for storing energy at large scales. This approach could mitigate the challenges of intermittency challenges associated with renewable energy sources. Solving the intermittency problem paves the way for widespread renewable energy adoption and reducing our dependence on carbon-emitting sources. Alternatively, SOFCs are good candidates for energy applications with high-reliability constraints, such as hospitals and centers.

The high operating temperatures (>900 °C) of conventional SOFCs require expensive interconnects, lead to long ramping times, and accelerate degradation mechanisms. Lowering the temperature to an intermediate range (500–750 °C) is paramount to their commercial viability; however, reducing temperatures typically penalize efficiency. The oxygen reduction reaction (ORR) in the cathode is generally considered performance-limiting at lower temperatures by requiring large overpotentials for the reaction to proceed at required rates. Material properties and relevant phenomena in the cathode fundamentally govern these rates and must be understood before further electrode optimization.

1.1 SOFC MATERIALS

1.1.1 *Mixed Conducting Cathodes*

Mixed ionic electronic conducting (MIEC) perovskites are widely studied as oxygen reduction electrode materials. In contrast to materials with limited ionic or electronic conductivity, ORR in MIECs can extend far away from the triple phase boundaries–where gas, electrode, and electrolyte meet. Increasing the total active area of the electrode enhances the overall performance.

We chose to study the $ABO_{3-\delta}$ perovskite $La_{1-x}Sr_xCoO_{3-\delta}$ (LSC), with x=0.4, as a suitable cathode material for intermediate temperature SOFC (IT-SOFC). Figure 1.1shows an illustrated crystal structure of LSC. Replacing La^{3+} with Sr^{2+} at the A-site is partially compensated by Co valence

changes at the B-site and vacancies formed at oxygen lattice sites. ORR in LSC is mediated by surface vacancies, whereas bulk vacancies provide the pathway for ionic conduction.

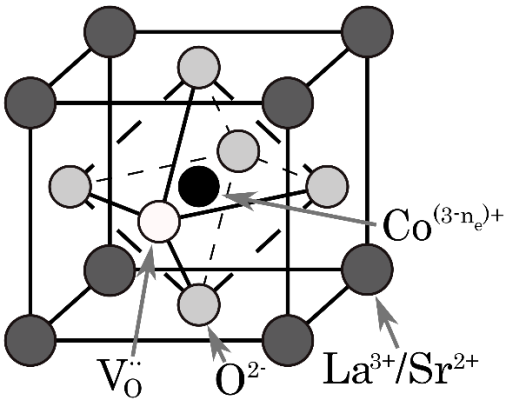

Figure 1.1. Crystal structure of $La_{1-x}Sr_xCoO_{3-\delta}$.

Figure 1.2 illustrates the possible pathways for ORR in a porous MIEC electrode. First, O_2 must diffuse to the surface (a), followed by a surface exchange reaction (b). An O atom is either: (c.i) fully reduced and incorporated into the material for bulk transport, or (c.ii) partially reduced and transported along the surface. Finally, O ions transfer into the electrolyte (d).[1] Limitations from steps (a) and (d) are avoidable through electrode design and electrolyte choice, respectively. In contrast, the specific thermodynamic, kinetic, and transport properties of the material control the rates of (b) and (c). The limiting steps and relative rates of these processes dictate the size of the active region and the overall performance.

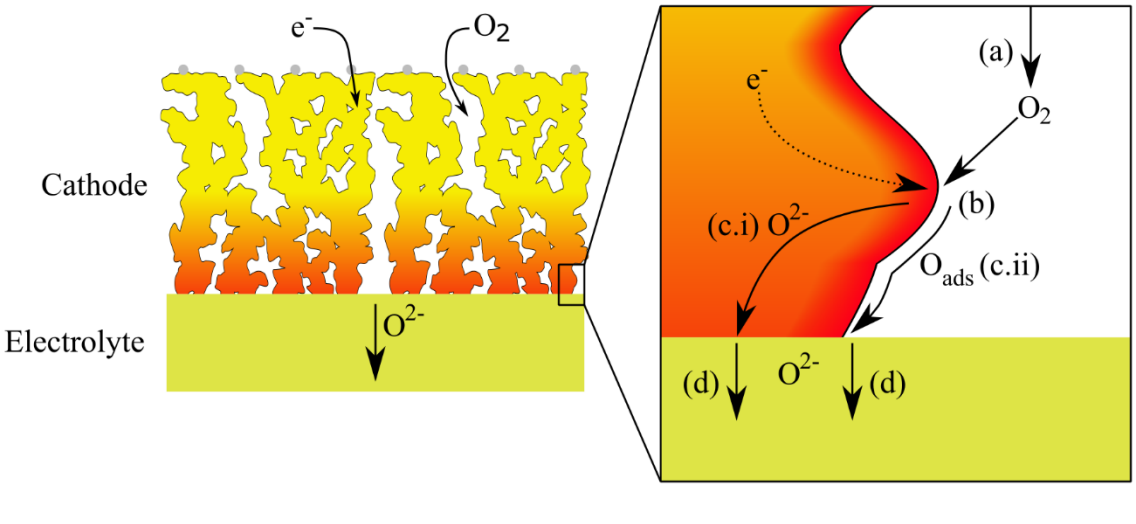

Figure 1.2. Pathways for oxygen reduction in porous $La_{1-x}Sr_xCoO_{3-\delta}$ electrodes.

Previous studies investigated the material properties across a range of Sr content, sample morphologies, and operating conditions using linear and nonlinear impedance spectroscopy to investigate the material properties.[2–5] Each example interprets the measured impedance through increasingly sophisticated descriptions of dimensionality, cation distribution, and microstructure. The models were qualitatively consistent with the measured responses, and the authors suggest further refinements to approximations in the analysis to account for discrepancies. Even nominally model systems using thin films exhibit unique–and sometimes inconsistent–behavior. Their work revealed surprising insights about ORR in LSC and emphasized the challenges of reaching fundamental knowledge without knowing local chemistry in the tested environment.

1.1.2 *Electrolytes*

An SOFC electrolyte material should have high ionic conductivity and low electronic conductivity at the operating temperature and stable in oxidizing and reducing conditions. Additionally, it should be chosen with the anode and cathode materials in mind to match thermal expansion coefficients and avoid reactivity between the components.

The fluorite oxides zirconia and ceria are popular choices for their ionic conductivities. In these systems, mobile oxygen vacancy defects provide the pathway for oxygen diffusion. The oxides are generally doped with a lower valence cation to establish extrinsic defect levels. Zirconia is typically doped with yttria (YSZ), whereas gadolinia and samaria are common dopants for ceria (GDC, SDC). YSC shows high ionic conductivity at temperatures >700 °C and is stable over a wide pO_2 range; however, it tends to react with La-based cathodes.[6,7] Ceria exhibits sufficient ionic conductivity at even lower temperatures (500 °C) and is less reactive with La-containing perovskites.[8] However, it becomes electronically conductive at reducing pO_2 experienced on the anode side.[9–11] Given our focus on oxygen reduction in LSC, we restrict further discussion to ceria.

Ohmic losses through the electrolyte can be minimized by increasing the conductivity or reducing the thickness, given material properties and mechanical stability requirements. The appropriate thickness is further complicated by size-dependent conductivity in ceria, where smaller grain size correlates with dramatic shifts in ionic and electronic conductivities.[12–14] Workers proposed a space charge region (SPR) model to explain size effects, where positive charge trapped at grain boundaries leads to vacancy depletion and electron enrichment.[15–18] The model captures

important features of the behavior, but length scales and extents of depletion in SPRs derived from bulk measurements remain ambiguous.[19,20] Improving our understanding of SPRs in ceria enables further optimization to reduce SOFC performance losses associated with the electrolyte.

1.2 Measurement Techniques

The literature cited above represents a "top-down" approach, where workers compare a proposed model for the local behavior to measurements representing an average response across the whole sample geometry. The effort and expertise needed to reach unambiguous conclusions in even a simplified system is unscalable when considering the range of candidate materials for IT-SOFCs.

Here, we propose the inverse, "bottom-up" approach where the local response is directly measured and used to determine material properties. Then, a model can be scaled to the full sample geometry and compared with the global response. This work focuses on developing the techniques and tools to determine electrochemical behavior spatiotemporally at the micro- and nanoscales.

1.2.1 *X-ray Absorption Spectroscopy*

X-ray absorption spectroscopy (XAS) is an extremely versatile technique to probe the chemical environment of an atomic species. The simplified description below reflects the relatively limited approach to XAS we take in this work. We refer readers to reviews by Newville, and Henderson, de Groot, and Moulton for more detailed explanations.[21,22]

Although several processes can occur when an X-ray interacts with matter, the discussion here is limited to X-ray fluorescence. XAS uses the photoelectric effect to probe the electronic state of an absorbing atom. An X-ray photon excites a core electron out of an atom when the incident photon energy is greater than or equal to the electron binding energy. Core electron binding energies are discrete, leading to large absorption changes (edges) at energies where the X-ray photon is successfully absorbed. After the ejection of a core electron, a higher-energy core electron relaxes to the resulting core-level hole. A photon with energy equal to the difference between the two energy levels because of energy conservation. Since the energy of core electrons are characteristic of each element, a material is identifiable by measuring the energies where

absorption edges occur. Electron binding energies also depend on an atom's oxidation state, leading to changes in the absorption edge energy.

We primarily describe XAS the energy-dependent absorption coefficient, μ(E). In fluorescent mode XAS, μ(E) is given by:

$$\mu(E) \propto \frac{I_f}{I_o} \tag{1.1}$$

Where I_o is the incident X-ray intensity, and I_f is the fluoresced X-ray intensity. In practice, the energy dependence is found by tuning the incident X-ray energy via a monochromator to give a narrow energy band. Measurements within approximately 30 eV of the absorption edge are called near-edge spectra (XANES). Figure 1.3 shows XANES spectra measured on a dense thin film LSC electrode under open-cell conditions and polarization. Applying a voltage to the film reduces or oxidizes the electrode and shifts the average oxidation state, seen by absorption edge shifts. Taking the difference in XANES spectra at applied bias and OCV highlights the effect. The difference spectra reveal X-ray energies around 7720 eV are most sensitive to vacancy concentration shifts for this sample.

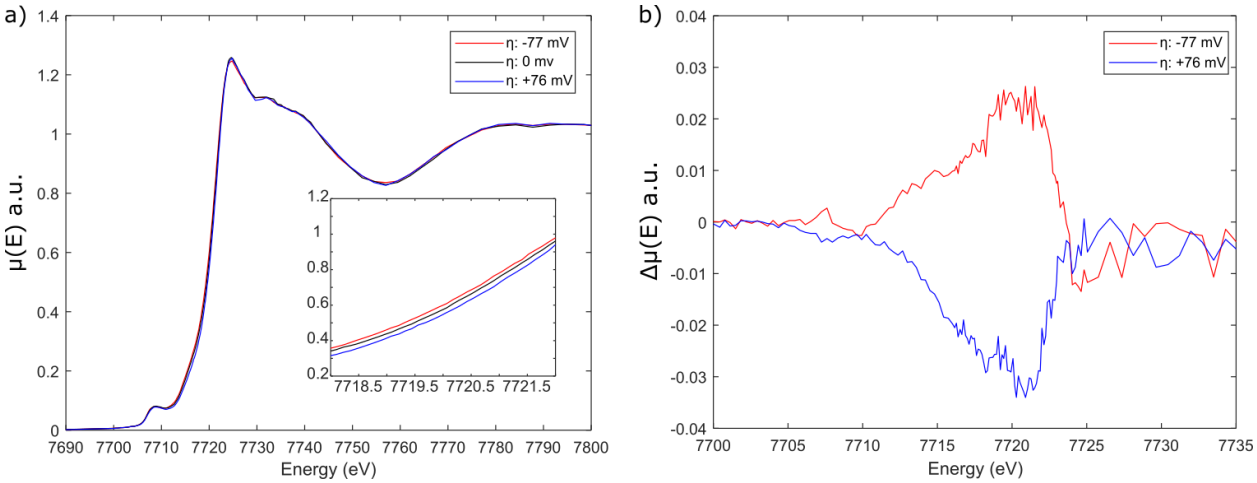

Figure 1.3. XANES spectra (a) and difference spectra (b) of an LSC thin film at 700 °C in 0.10 bar O2.

XAS reflects the response integrated over the exposed volume of material. Spatial gradients can be resolved by changing the sample position relative to the incident beam. Specialized optics available at some dedicated synchrotron beamlines focus the incident beam to achieve high spatial

resolutions; however, this reduces the fluoresced X-ray intensity because a smaller volume of material is probed. Spot sizes in this work are typically 600 nm x 300 nm for sub-micron resolution.

1.2.2 *Scanning Probe Microscopy*

The atomic force microscope (AFM) was introduced in 1986, combining scanning tunneling microscopy and profilometry.[23] At its core, AFM detects Van der Waals forces between a cantilever with an atomically sharp tip and a sample surface to probe features with nanometer resolution. A laser reflected off the cantilever surface measures the cantilever deflection, which indicates forces imparted on by the cantilever if the stiffness and dimensions are known. A precise positioning system controls the distance between the tip and surface using the deflection signal as feedback. AFM is typically used to measure sample topography by adjusting the probe height to maintain constant deflection and rastering the tip in an x-y grid.

A multitude of functionalities generally called scanning probe microscopies (SPM) emerged from this platform to study electrostatic and magnetic forces above a sample, including but not limited to Kelvin probe force microscopy (KPFM), piezoelectric force microscopy (PFM), and electrostatic force microscopy (ESM). As discussed in Chapter 4, conductive probes can be used to apply an electric field to the sample and induce strain in the material below the tip. Applying the electric field with an AC wave at the sample's mechanical resonance frequency amplifies the strain to more easily detected levels. This effect is the basis of PFM and ESM, which are identical in practice but use different names to identify distinctive electromechanical and electrochemical origins of the strain. Studying the phase of the response with respect to the applied voltage and the presence of higher-order harmonic responses are used to characterize the underlying physics. In principle, ionic concentrations are measurable by calibrating the strain response with a sample of known composition.

1.2.3 *Electrochemical Impedance Spectroscopy*

Electrochemical impedance spectroscopy (EIS) uses small amplitude AC signals (either current or voltage) to probe physical processes in electrochemical systems. The signal perturbs the system over several waveforms at each frequency until the response is steady-periodic and subsequently recorded by phase-sensitive detection. Modern implementations use the Fast Fourier Transform

algorithm (FFT) for converting the time-domain signals into the frequency domain where the complex Fourier coefficients define the phase and magnitude relative to the input. The ratio of voltage and current complex Fourier coefficients defines the impedance. For a voltage perturbation of radial frequency ω, this is given by:

$$Z(\omega) = Z' + jZ'' = \frac{V'}{i' + ji''} \tag{1.2}$$

Figure 1.4 shows the simulated EIS data on a Nyquist plot. A Nyquist plot is common for representing EIS data, where the imaginary component is plotted against the real component, and the data is parametric in frequency. The simulated data emulates a porous MIEC electrode with three serial process well separated by timescale: a high frequency intercept representing ohmic resistance, a semicircular arc with characteristic frequency ω_c representing an interfacial charge transfer reaction, and a Gerischer shape at low frequency representing an electrode co-limited by ion transport and surface exchange. Each feature is defined by the shape, width, and characteristic frequency, which is straightforward in this example. EIS isolates processes by timescale at the inverse of the applied frequency. However, the linearized EIS makes it challenging to identify non-uniform thermodynamic, transport pathways, and mechanisms of rate-limiting kinetic steps. Furthermore, complex microstructures or spatially inhomogeneous material process can lead to a distribution of timescales, resulting in distorted or depressed EIS features.

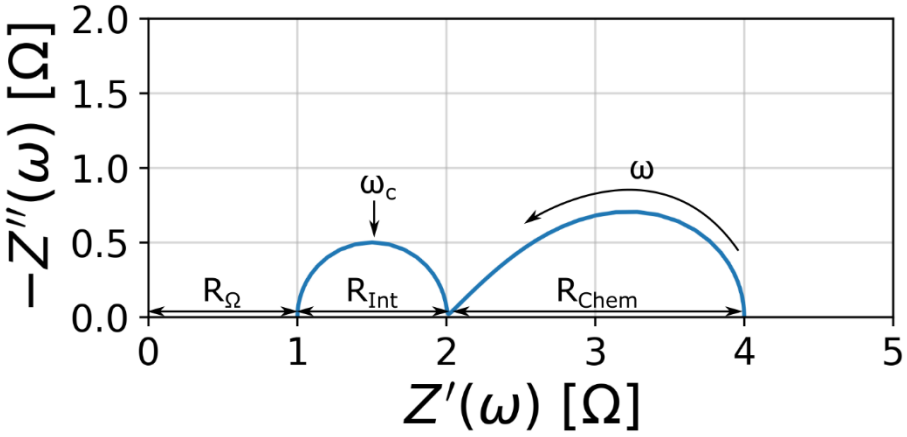

Figure 1.4. Nyquist plot of simulated EIS data representing ohmic resistance (R_Ω) in series with a kinetically limited process (R_{Int}) and a co-limited, Gerischer process (R_{Chem}).

Chapter 2. DYNAMIC X-RAY SPECTROSCOPY OF LSC-64 THIN FILM ELECTRODES[1]

2.1 INTRODUCTION

Transition-metal oxide perovskites are promising for use solid oxide fuel cell (SOFC) electrodes, gas sensors, oxygen separation devices and ceramic membranes reactors. Their promise arises from mixed electronic and ionic conducting properties which extends the electrochemically active portion of an electrode by providing an oxygen vacancy transport pathway. In particular $La_{1-x}Sr_xCoO_{3-\delta}$ has been widely studied as an oxygen electrode for its high oxygen ion conductivity and large nonstoichiometry at intermediate temperatures leading to a general understanding of the bulk thermodynamics.[1,24] However, previous work showed bulk material used for porous electrodes behaves substantially different than thin film electrodes used to isolate kinetics, pointing to possible differences in *local* thermodynamics.[3,25,26] This necessitates development of techniques sensitive to local chemistry with access to temperatures and gas environments relevant to SOFC operation. Furthermore, the ability to selectively probe processes based on time scale, as with impedance spectroscopy, is highly advantageous. This work demonstrates the first step towards such a technique extending previous developments of *operando* micro XAS (*operando* μ-XAS) to the frequency domain.[27–29]

XAS is a useful tool for investigating high temperature material *in situ* as it does not require specific experimental conditions and provides extensive element-specific information about the chemical and physical environment around a probe atom.[21] The absorption edge of a transition-metal is highly sensitive to electronic state, which is closely correlated to its mean oxidation state, resulting in positive energy shifts at higher mean valence states.[27,30] The mean valence state of Co in LSC shifts to compensate for oxygen vacancies introduced by the following defect equilibrium expressed in Kröger-Vink notation:

$$O_O^X + 2Co_{Co}^{\bullet} \rightleftharpoons O_2(g) + V_O^{\bullet\bullet} + 2Co_{Co}^X \tag{2.1}$$

[1] This is the Accepted Manuscript version of an article accepted for publication in ECS Transactions. The Electrochemical Society and IOP Publishing Ltd are not responsible for any errors or omissions in this version of the manuscript or any version derived from it. The Version of Record is available at https://doi.org/10.1149/09101.1387ecst

Therefore, the oxygen chemical potential can be effectively measured by energy shifts in the Co K-edge absorption spectra, where shifts to lower energy indicate lower oxygen potential and partial reduction of the oxide.

2.2 Experimental Methods

Collaborators from Tohoku University—Keita Mizuno and Shota Kageyama—synthesized and prepared the thin film samples and electrochemical cells used in this work. Spring-8 beamline scientists Dr. Oki Sekizawa and Dr. Kiyofumi Nitta assisted with X-ray measurements.

2.2.1 *Thin Film Electrochemical Cell*

Approximately 3g of $Ce_{0.9}Gd_{0.1}O_{1.95}$ powder (GDC, Shin-Etsu Chemical Co., Ltd.) was uniaxially pressed in 20 mm diameter die followed by hydrostatic pressing at 200 MPa. The pellet was then sintered at 1550 °C for 5 hours to produce an approximately 3 mm thick pellet with an approximate diameter of 16 mm and 97% of theoretical density. One side of the pellet was mirror-polished (performed by Disco, Inc.) to an average surface roughness of 2.0-5.0 nm. A counter electrode was painted on the unpolished surface by mixing Pt paste (Tanaka Kikinzoku Kogyo Co., Ltd.) and LSC64 powder (AGC Seimi Chemi) in a 6:4 weight ratio. The counter electrode was then fired at 950 °C for 3 hours. A thin film electrode was then deposited on the polished side of the pellet by pulsed laser deposition (PLD, YAG laser, 180 mW) under 10^{-5} bar O_2 and a substrate temperature of 800 °C. The thin film was then annealed at 800 °C for 4 hours under 1 bar O_2. The resulting film was approximately 570 nm thick and 13 mm in diameter. Finally, the sample was cut down a cube roughly 3 x 3 x 3 mm in size and a Pt reference electrode was painted around the bare sides.

Electrochemical impedance spectroscopy (EIS) was measured potentiodynamically using a Bio-Logic SP-150 potentiostat with a 20 mV perturbation amplitude with frequencies spanning 1 kHz to 17 mHz. Measurements were collected while the sample was in an *operando* micro XAS holder, as detailed in[28,31] , under a 10% O_2 balance N_2 gas environment at 973 K.

2.2.2 *Dynamic operando X-ray Absorption Spectroscopy (XAS)*

Using a custom built sample holder fabricated by co-workers at Tohoku University, fluorescence mode XAS measurements were carried out at the BL37XU beam line, Spring-8, JASRI, Japan.[28,31]

At this beam line, the incident X-ray can be focused to a micro or sub-micrometer spot size using a Karkpatric-Baez mirror. Incident X-ray energies spanned 7600 eV to 7845 eV. Fluoresced X-rays were collected by a photodiode and incident X-rays were collected by an ion chamber. Analog signals from the fluoresced and incident X-rays were collected synchronously with current and voltage signals from the SP-150 potentiostat by two National Instruments 5922 oscilloscopes. Custom LabVIEW software was written to carry out the measurements.

2.3 RESULTS & DISCUSSION

2.3.1 *Electrochemical Impedance Spectroscopy*

Figure 2.1shows the EIS spectrum collected at 973 K in 10% O_2 with no applied bias. A slightly depressed semi-circle is observed indicating the electrode is kinetically limited. A simplified Randles circuit with a constant phase element was fit to the data resulting in values of 64.2 Ω, 47.2 Ω, 9.41×10^{-3} $F \cdot s^{0.935}$ for R_s, R_c, and CPE, respectively. This approach is used primarily to facilitate frequency-dependent overpotential calculations for the voltage perturbations according to:

$$\eta(t) = \tilde{V}(t) - i(t)R_s \tag{2.2}$$

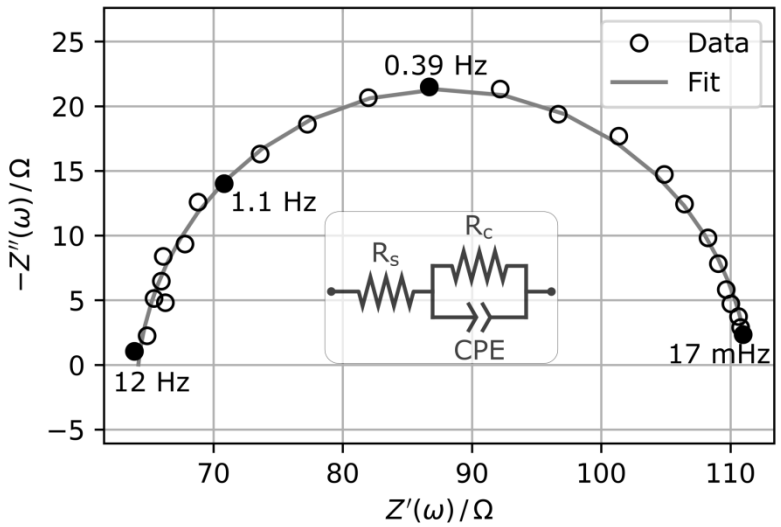

Figure 2.1. The EIS spectrum of the thin film at 973 K in 10% O_2 shows a slightly depressed semi-circular shape, suggesting kinetic limitations. Data is fit to the simple Randles circuit shown in the inset.

2.3.2 *Dynamic operando X-ray Absorption Spectroscopy*

Figure 2.2 shows Co K-edge X-ray absorption spectra observed for the LSC electrode at 973 K in 10% O_2 at many points (overpotentials) along a perturbation cycle for applied frequencies 0.5, 1, and 5 Hz. Note the spectra have not been normalized and flattened to pre-edge and post-edge lines. At cathodic (negative) overpotentials, the absorption edge shifts towards lower energies relative to the unbiased state, whereas at anodic (positive) overpotentials the edge shifts to higher energies. These results qualitatively agree with previous steady-state measurements connecting Co absorption edge shifts to changes in mean Co oxidation state to compensate oxygen vacancy concentration shifts.[27,30,31] As the perturbation frequency increases the absorption edge excursions narrow and the range of overpotentials also decreases. The latter is a consequence of controlling total cell voltage.

Figure 2.3 shows the relative (mean subtracted) absorbance at 7720 eV incident X-ray energy for all three perturbation frequencies as functions of the applied overpotential where positive values indicate absorption edge shifts to lower energies. The trends for absorbance excursions and overpotential range seen in Figure 2.2 hold true here as this is simply another perspective on the same data. The slope is lowest for 5 Hz and highest for 0.5 Hz, though the 0.5 Hz and 1 Hz slopes are nearly identical. These slopes relate how strongly the XAS spectra is shifting independent of the overpotential range. Theoretically the absorbance should fall on a single line as the overpotential sweeps through a perturbation cycle; however, the data have some ellipsoidal character. One explanation is a phase lag arising from bulk vacancy diffusion through the film thickness and the volume-averaged nature of XAS measurements.

As the vacancy concentration at the electrolyte/electrode interface is modulated by the overpotential, vacancies must diffuse through the film to the gas-exposed surface. When the characteristic time for diffusion isn't fast compared to the perturbation, a concentration profile develops perpendicular to the film resulting in dissimilar absorbances at a given overpotential depending on the cycle phase. Using the 570 nm electrode thickness and assuming a vacancy diffusion coefficient of 10^{-7} cm^2/s gives rise to a characteristic diffusion time of 32.5 ms.[2] This time corresponds to phase lags of 5.9, 11.7, and 58.5° for the 0.5, 1, and 5 Hz perturbations, respectively. In accordance with this theory 1 Hz is wider than 0.5 Hz; however, 5 Hz does not open as expected.

The narrow absorbance excursions and small slope for 5 Hz seen in Figure 2.2 and Figure 2.3, respectively, indicate only small shifts in the Co valence state and therefore oxygen potential in the oxide. Since 5 Hz is close to the high-frequency intercept in Figure 2.1, this suggests the timescale is too fast to significantly activate oxygen kinetics. On the other hand, the 0.5 and 1 Hz perturbations show the wide excursions in Figure 2.2 and high slopes in Figure 2.3 indicating the oxygen potential is modulated considerably. Again, these results are consistent with EIS in Figure 2.1, where 0.5 and 1 Hz are considerably higher on the depressed semicircle suggesting oxygen kinetics are engaged at those timescales. In fact, the XAS results support the impedance interpretation as it represents a direct measure of the faradaic reaction.

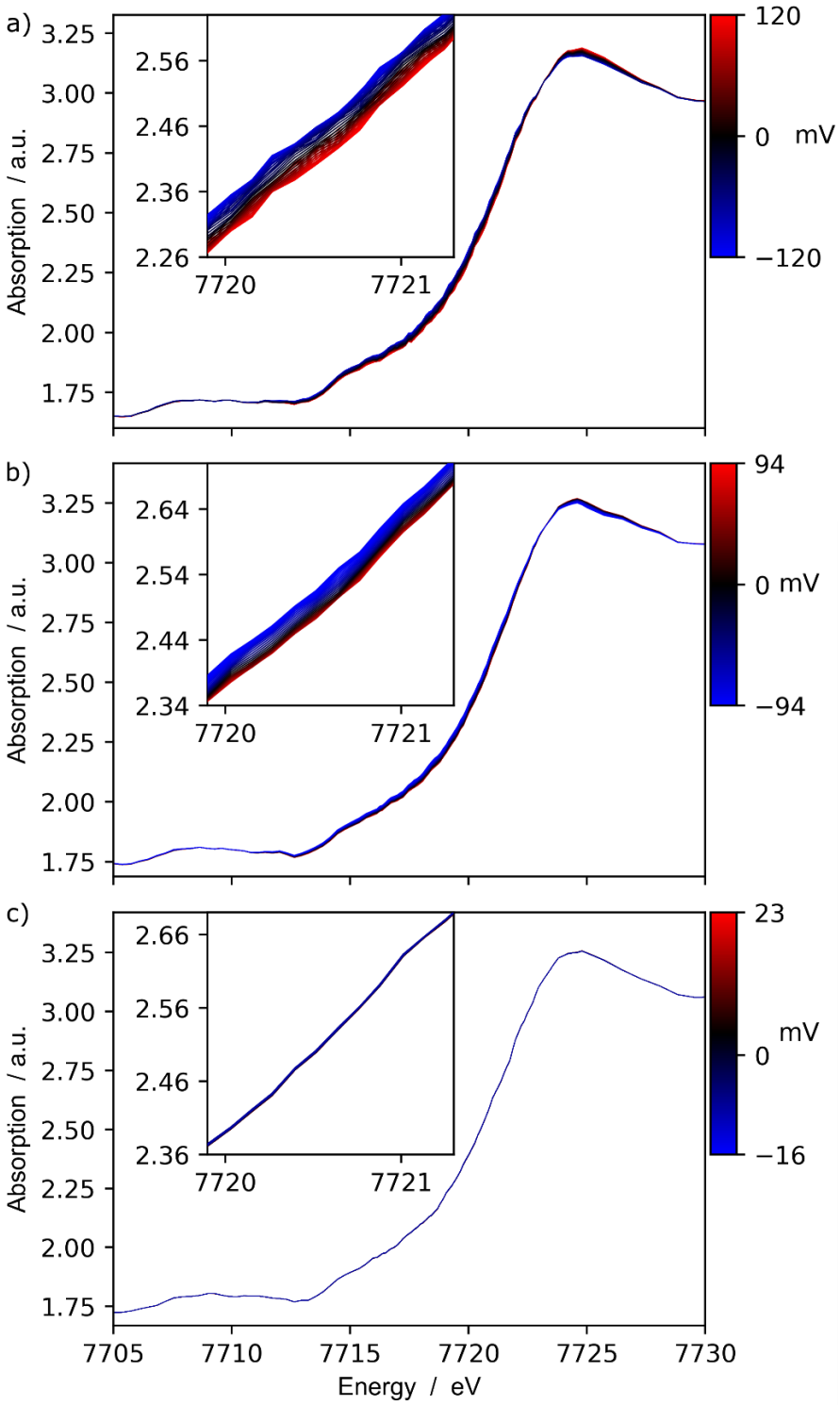

Figure 2.2. *In-situ* micro XAS spectra of Co *K*-edge of $La_{0.6}Sr_{0.4}CoO_{3-\delta}$ under a) 0.5 Hz, b) 1 Hz, and c) 5 Hz voltage perturbation in 10% O_2 at 973 K. Lines represent the spectrum at a single overpotential in the sinusoidal perturbation, as indicated by color where red are anodic (positive) and blue are cathodic (negative) overpotentials.

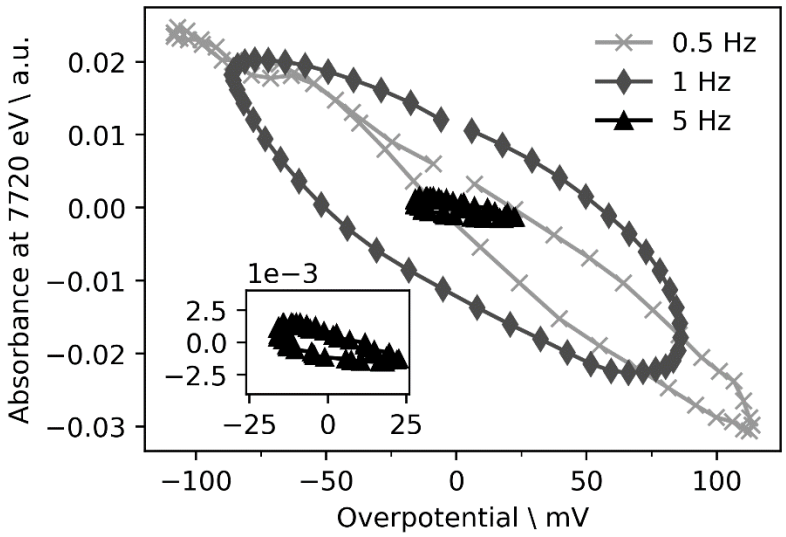

Figure 2.3 Relative X-ray absorbance at 7720 eV incident X-ray energy for 0.5, 1 and 5 Hz voltage perturbation frequencies. Inset is an expanded view of 5 Hz data.

2.3.3 *Local Structure*

Figure 2.4 shows the magnitude of Fourier transformed XAFS weighted by k^2 (FT[$|\chi k^2|$]) around the Co atom in LSC64. This reveals the coordination and bonding distances around Co from photoelectron scattering by neighboring atoms.[21] Lateral shifts in peak position indicate changes in bond length while shifts in intensity may relate to electron density around the absorbing Co atom.[21] The peaks around 1-2 Å are attributed to first neighbor Co-O pairs whereas peaks around 3-4 Å correspond to second neighbor Co-(La,Sr) and third neighbor Co-Co pairs.

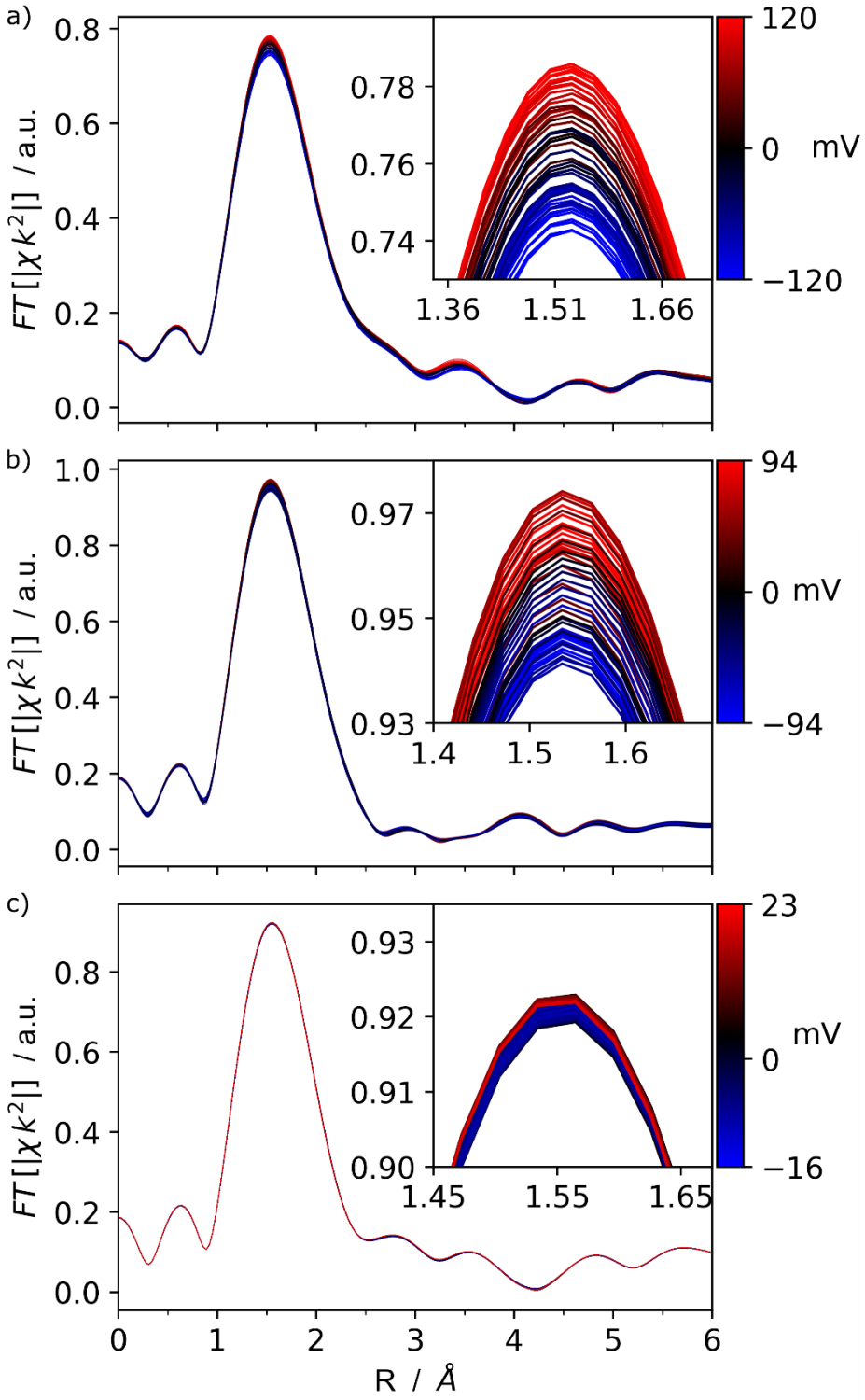

Figure 2.4 Magnitude of Fourier transformed XAFS around Co atoms in $La_{0.6}Sr_{0.4}CoO_{3-\delta}$ under a) 0.5 Hz, b) 1 Hz, and c) 5 Hz voltage perturbations in 10% O_2 at 973 K. Lines represent the RDF at a single overpotential in the sinusoidal perturbation, as indicated by color where red are anodic (positive) and blue are cathodic (negative) overpotentials.

As with Figure 2.2, each line represents the FT[|χk^2|]) for a single overpotential in the perturbation cycle. The FT[|χk^2|]) peaks around 1.5 Å for 5 Hz are essentially insensitive to the overpotential, whereas those for 0.5 Hz and 1 Hz significantly shift in amplitude. Notably, the peaks do not observably shift laterally, indicating bond lengths are effectively unchanged despite observable oxidation state shifts in Figure 2.2. This disparity is rationalized by chemical expansion in LSC which arises from changes in Co-O bond length as vacancies are introduced to the material. [32] Uniaxial strain for an isotropic solid is given by

$$d\varepsilon = \tfrac{1}{3}\beta_t dT + \tfrac{1}{3}\beta_c dx_v \tag{2.3}$$

Where ε, β_t, T, β_c, and x_v are the uniaxial strain, thermal expansivity, temperature, chemical expansivity, and oxygen vacancy mole fraction, respectively. Let us consider isothermal strain arising from chemical expansion taking ⅓ $\beta_c \approx 0.1$ ppm/ppm [32,33]. The shift in x_v for 0.5 Hz is estimated to be ~8% from $\partial \ln x_v = (-\tfrac{1}{2A})\partial \ln pO_2$ with $\partial \ln pO_2 = -5$, and assuming A≈2 and $x_{v,o}$=0.02. Therefore, the estimated shift in bond length is only 0.8%! Moreover, if the film is not diffusionally equilibrated, as suggested earlier, the peak would broaden at intermediate frequencies and obscure small shifts in the peak position.

On the other hand, the peak amplitude modulations may arise from changes in the scattering properties of the photoelectron (i.e. electron density surrounding Co) or Co coordination; however, distinguishing between these effects is complicated due to correlation of the factors. [21] If we assume coordination number changes are dominant, the 4% amplitude shift, and therefore coordination number, for 0.5 Hz only accounts for 0.7% change in x_v. The inconsistency motivates measurements across a broader energy range to confidently resolve the fine structure.

2.4 SUMMARY

Dynamic changes in the electronic and local structures of $La_{0.6}Sr_{0.4}CoO_{3-\delta}$ dense thin films were studied by measuring Co K-edge XAS during sinusoidal voltage perturbations. Absorption edge shifts qualitatively agreed with previous works; however, this approach revealed smooth transitions in Co oxidation state over several orders of magnitude in pO_2. Different timescales of processes were probed by varying the voltage perturbation frequency showing oxygen kinetics respond strongest at 0.5 Hz in agreement with EIS results. Although the Co-O bond length changes with oxygen vacancy concentration, such shifts in local structure were immeasurable in the Fourier transformed XAFS. Amplitude shifts observed in the local structure were inconsistent with changes in Co coordination; however, we need measurements across at energies further above the absorption edge and with better resolution to be confident in our analysis. Altogether, we demonstrated a frequency-resolved method of XAS as a chemically-sensitive tool for detecting electrochemical responses and isolating by timescale.

Chapter 3. IMAGING OXYGEN VACANCY DISTRIBUTIONS IN LSC USING FREQUENCY-RESOLVED X-RAY ABSORPTION SPECTROSCOPY

Development of materials for electrochemical energy conversion requires a deep understanding of the factors governing chemical and physical rates at submicron length scales. Many workers have sought to develop chemically sensitive in situ or operando imaging techniques targeting these length scales. However, current methods focus on steady-state or stepwise response. To probe electrode processes both spatially and temporally, we have developed a frequency-resolved implementation of X-ray absorption imaging (FR-XAS) that can measure local electrochemical response in operando during a global sinusoidal impedance perturbation. Using this method, we acquired frequency-resolved 1D images of the oxygen vacancy distribution in a thin film SOFC cathode material ($La_{1-x}Sr_xCoO_{3-\delta}$) during an impedance measurement. These images reveal, for the first time experimentally, the defect concentrations associated with a Warburg and Gerischer impedance. Analysis of these images allows direct extraction of diffusion and kinetic rate parameters, independent of the global impedance, which in this system is convoluted by other factors.

3.1 MOTIVATION

Electrochemical impedance spectroscopy (EIS) is often used to probe rates in electrochemical systems as a function of timescale. However, as with any electrochemical measurement, EIS represents the aggregate response of the system, which is an average of rates over the entire sample geometry. Unambiguously attributing local processes to EIS features is challenging, particularly in samples with inhomogeneous properties.[1,34]

Over the last 30 years,workers have developed a variety of chemically sensitive in situ and operando methods to allow direct measurements of rate phenomena in electrochemical systems with spatial and/or chemical specificity.[35] For example, Lim et al. used operando scanning transmission X-ray microscopy to image intraparticle intercalation pathways in Li-ion battery cathodes during dis/charge cycles.[36,37] As another example, Tada et al. directly probed the kinetics of redox processes on Pt catalysts using operando time-resolved X-ray absorption fine structure.[38–

[40] Although these examples involved nonstationary behavior, an inherent limitation of stepwise response is that it simultaneously probes a broad range of timescales.[41,42] In many systems we'd like to selectively probe the response at specific frequencies, both to isolate particular rates, as well as to more directly relate operando observations to impedance measurements. This builds on previous efforts determining effective reaction areas under steady-state polarization with micro X-ray absorbance spectroscopy (μ-XAS)—by extending these methods into the frequency domain.[28]

3.2 PATTERNED ELECTRODES

This work focuses on the mixed ionic-electronic conducting (MIEC) cathode $La_{0.6}Sr_{0.4}CoO_{3-\delta}$ (LSC) often studied as a model electrode for O_2 reduction/oxidation in high temperature electrochemical systems and devices.[1] As shown in Figure 3.1a, the oxygen reduction reaction (ORR) in a typical porous electrode is thought to occur by a combination of steps that may proceed in series or parallel. Due to these parallel rates, as well as uncertainties in electrode microstructure and material properties, interpretation of the global impedance response in this system is notoriously difficult.[1] In order to mitigate uncertainties associated with microstructure and variations in properties, as well as provide access to the electrode surface by chemical probes, a number of workers (including the co-authors) have developed electrodes based on patterned thin films.[28,43,44] As shown in Figure 3.1b, ORR in a patterned thin film proceeds by the some subset of the same reactions steps, but involves surfaces and bulk transport pathways having well-defined geometry. It remains an open question whether the surface and bulk properties of such films match those of materials in a porous electrode.[3,26,45] Addressing this question is a significant motivation for the present work.

As illustrated in Figure 3.1b, the extended surface area of a porous electrode is emulated in a thin film by limiting electrode/electrolyte contact to a narrow region called the electrode "gates".[28] This is achieved by laser-depositing an insulating layer of amorphous Al_2O_3 onto a polished polycrystalline Gd-doped CeO_2 electrolyte pellet, lithographically removing portions of specified dimensions, and laser-depositing a thin LSC film on top.[28] Figure 3.1c and d show electrode gates are formed where gaps in the insulating layer are conformally filled by LSC.

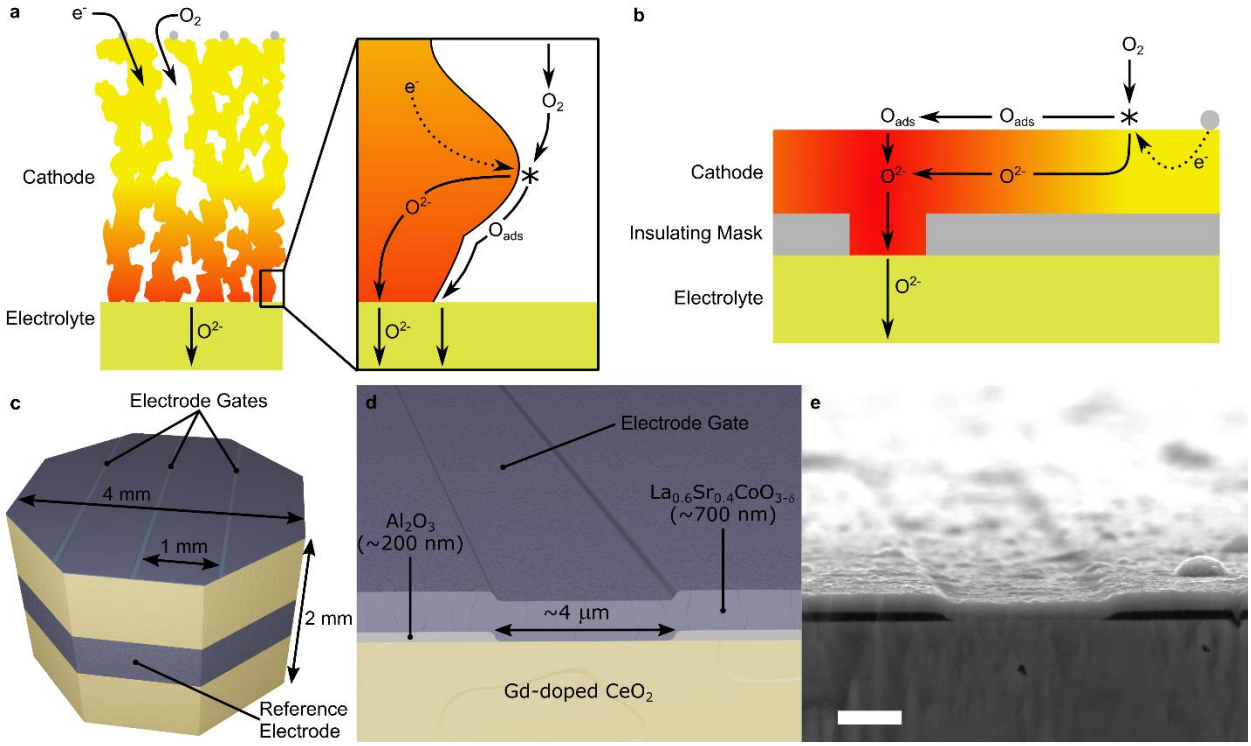

Figure 3.1. **a**, Schematic showing the possible pathways for oxygen reduction on a porous mixed ionic-electronic conductor. **b**, Schematic showing the possible pathways for oxygen reduction on a patterned thin film electrode. **c**, Schematic showing typical dimensions of a patterned thin film sample with three electrode gates studied with FR-XAS. **d**, Schematic showing typical dimensions of thin film layers and an electrode gate. **e**, SEM image of electrode gate studied in this work. Scale bar, 2 µm.

The LSC film only contacts the electrolyte along these gates but is exposed to the gas over the entire top surface. The resulting geometry can be thought as a porous electrode laid on its side, with the gas-exposed surface accessible to incident and fluoresced X-rays. Electrode gates are separated by 1 mm to avoid overlap of vacancy gradients—spanning at most 200 µm—from adjacent gates. Typical film thicknesses are 400–800 nm and 150–300 nm for the electrode and insulating layers, respectively. The electrolyte pellet is approximately 2 mm thick and 16 mm in diameter during film deposition, after which is cut into cuboids about 4 mm in width and height. Finally, the cuboids are trimmed into octagonal prisms to fabricate electrochemical cells for operando characterization.

3.3 EXPERIMENTAL METHODS

Collaborators from Tohoku University—Keita Mizuno and Shota Kageyama—synthesized and prepared the patterned thin film samples and electrochemical cells used in this work. Spring-8 beamline scientists Dr. Oki Sekizawa and Dr. Kiyofumi Nitta assisted with X-ray measurements.

3.3.1 *Patterned Sample Fabrication*

The patterned thin film sample was prepared using pulsed laser deposition (PLD) on a dense $Gd_{0.1}Ce_{0.9}O_{1.95}$ (GDC) pellet electrolyte. The electrolyte was prepared by uniaxially pressing ~3 g of GDC powder (Shin-Etsu Chemical Co., Ltd) in a 20 mm diameter die. The resulting pellet was hydrostatically pressed at 200 MPa followed by sintering at 1550 °C for 5 hours. Upon sintering, the pellet shrank to ~16 mm in diameter with a 97% relative density. One side of the pellet was mirror-polished to a surface roughness of 2~3 nm (Disco, Inc.). The other side was painted with a 60/40 wt% LSC/Pt (AGC Seimi Chemical Co., Ltd./ Tanaka Kikinzoku Kogyo Co., Ltd., TR-7907) paste as a counter electrode and sintered at 950 °C for 3 hours. On the polished side an image reversal photoresist (Clariant International Ltd, AZ 5214E) was applied, exposed to masked UV light and developed with 2.38% TMAH (Tama Chemicals Co., Ltd.) resulting in ~2 μm wide strips separated by ~1 mm. An insulating layer of Al_2O_3 (Nikkato Co., SSA-S) was then deposited with PLD with the following deposition parameters: 180 mW quadruple Nd:YAG laser with λ=266 nm, 10 Hz pulse rate at room temperature under a p_{O2} of 10^{-5} bar for 2 hours. Then acetone was used to dissolve the photoresist strips and lift-off overlaying portions of the Al_2O_3 film before annealing in air at 900 °C for 3 hour. A 13 mm diameter LSC electrode was then deposited by PLD at 800 °C under a p_{O2} of 10^{-5} bar for 1.5 hours and annealed for 4 hours at 800 °C under a p_{O2} of 1 bar. The resulting sample had an LSC film ~600 nm thick on top of a ~200 nm thick Al_2O_3 film with ~4 μm wide regions of electrode/electrolyte double phase boundary (DPB) separated by 1 mm where the Al_2O_3 layer was lifted off. This sample was cut with a diamond saw into several 4 mm X 4 mm X 2 mm cubes to prepare electrochemical cells for FR-XAS measurements.

3.3.2 *Electrochemical Cell and Sample Holder*

Electrochemical cells were fabricated from the cubes of patterned thin film samples by feeding Pt wire through a dual-bore alumina tube with a Pt mesh spot welded as a current collector for the

counter electrode. Porous Pt ink was painted around the perimeter of the electrolyte and a Pt wire was wrapped as a reference electrode. A Pt/10% Rh wire was spot welded to the Pt reference electrode wire near the sample surface to create an S-type thermocouple; this positive lead of the thermocouple was left electrically floating during all electrochemical and X-ray measurements. Another Pt wire with Pt mesh was placed on the edge of LSC thin film as a current collector for the working electrode. A C-shaped alumina plate was cemented (Inorganic Adhesive D, Aron Ceramics) to the end of a single-bore alumina tube, attached over the smaller alumina tube (to maintain contact between the Pt mesh current collector and LSC electrode) and cemented in place. Resistance heating wire was coiled around the end of the larger alumina tube and cemented (Inorganic Adhesive D, Aron Ceramics) in place as a heating element. This assembly was then fed into a slip-on flange with alumina-insulated feedthroughs for the heating element leads and a gas outlet. Finally, the flange was connected to a custom-fabricated jacketed chamber with a Kapton film window to control the gas environment while maintaining X-ray transparency.

3.3.3 *X-ray Measurements*

All X-ray absorption spectroscopy measurements were performed at BL37XU of the Spring-8, JASRI synchrotron facility in fluorescence mode using the experimental set up illustrated in Figure 3.2. The energy of the incident X-ray beam was adjusted by a double crystal Si(111) monochromator and the beam was focused to 0.6 x 0.9 μm by a Karkpatric-Baez mirror. Co K-edge X-ray absorbance near edge spectroscopy (XANES) was performed using incident energies ranging from 7.6 to 7.85 keV. Incident beam intensity was measured with an ion chamber and fluoresced X-ray intensity was measured with two four-element silicon drift detectors (Vortex-ME4, Hitachi High-Technologies Corp.). XANES spectra at a DPB on the sample were collected at 700 °C under p_{O2}'s of 1, 0.1, and 0.01 bar, controlled by premixed O_2-He gas cylinders. XANES spectra were also collected under cathodic and anodic polarization—typically +/- 150 mV—using a VersaSTAT 3 potentiostat to evaluate the absorption edge shift as a function of the film oxidation state. *Operando* micro XAS (μ-XAS) measurements were performed at a fixed incident X-ray energy of 7719.8 eV under open circuit conditions and cathodic polarization to establish the steady-state oxygen potential distribution.

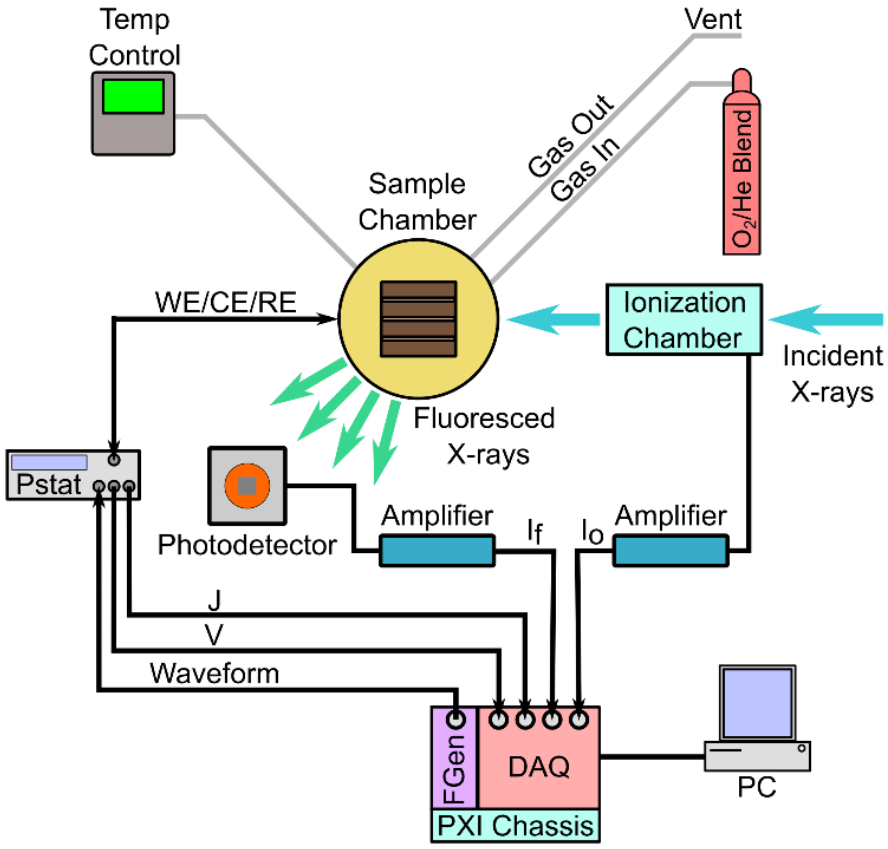

Figure 3.2. Schematic of FR-XAS experimental set up.

3.4 X-RAY SPECTROSCOPY AS A CHEMICAL PROBE

We use X-ray absorption spectroscopy (XAS) in this work to probe the local chemical and physical environment of an absorbing atomic species.[21,22] Figure 3.3a shows Co K-edge XAS spectra of thin film LSC at 700 °C under a pO_2 of 0.10 bar under open cell voltage and polarized conditions. Pre-edge features from 7707 to 7712 eV are attributed to electron state transitions permitted by hybridization of Co 3d and O 2p orbitals and are mostly insensitive to polarization.[30] The absorption edge (the energy where absorption is approximately 0.5) occurs near 7720 eV and shifts to lower energies under cathodic (negative) polarization. This is evidence of a chemical shift as cathodic polarization partially reduces the film and introduces oxygen vacancies that are charge compensated by changes in average Co valence.[30,46,47] As such, oxygen vacancy concentration is measurable via Co K-edge absorption.

Figure 3.3b shows the difference spectra of the data in Figure 3.3a using the spectrum at open cell voltage as the reference, which reveals an isosbestic point near 7723 eV. At energies between the pre-edge features and the isosbestic point, absorption increases (decreases) under negative (positive) polarization. At a single incident energy in this range, lateral translations of the edge energy (chemical shift) emerge as vertical absorbance modulations. Therefore, Co valence—and by extension vacancy concentration—is quantifiable by choosing a highly sensitive incident energy (e.g. 7720 eV). Measuring absorption at one energy over different physical locations and perturbation frequencies is the core principle of FR-XAS.

3.5 Principles of the Technique

FR-XAS measurements are performed by controlling cell voltage with a pure sinusoid perturbation while simultaneously recording electrochemical—voltage (V) and current (J)—and X-ray signals—incident flux (I_o) and fluoresced flux (I_f)—to maintain phase coherence. Data are collected at a fixed incident X-ray energy and perturbation frequency for one physical location. FR-XAS profiles are constructed by sweeping through a set of positions and perturbation frequencies determined by preliminary stead-state μ-XAS profiles and EIS spectra.

Figure 3.3c presents typical time-domain data collected during FR-XAS on an unpatterned thin film electrode. The top panel shows a 0.5 Hz voltage perturbation (closed markers) and corresponding overpotential (η; open markers) defined by $\eta = V - IR_\Omega$, where R_Ω is the electrolyte resistance. A dashed cyan line and dot-dashed green line are added to indicate troughs of the voltage and overpotential waves, respectively. The bottom panel shows X-ray absorbance (μ) at 7719.8 eV, where μ is the ratio of I_f to I_o, which exhibits a clear response to the voltage. As expected from XAS spectra under polarization, absorbance decreases as voltage increases; however, the dashed and dot-dashed lines reveal absorbance is 180° out of phase with overpotential not voltage. This occurs because overpotential, which experiences a frequency-dependent phase shift from current flowing through the cell, controls oxygen vacancy concentrations at the

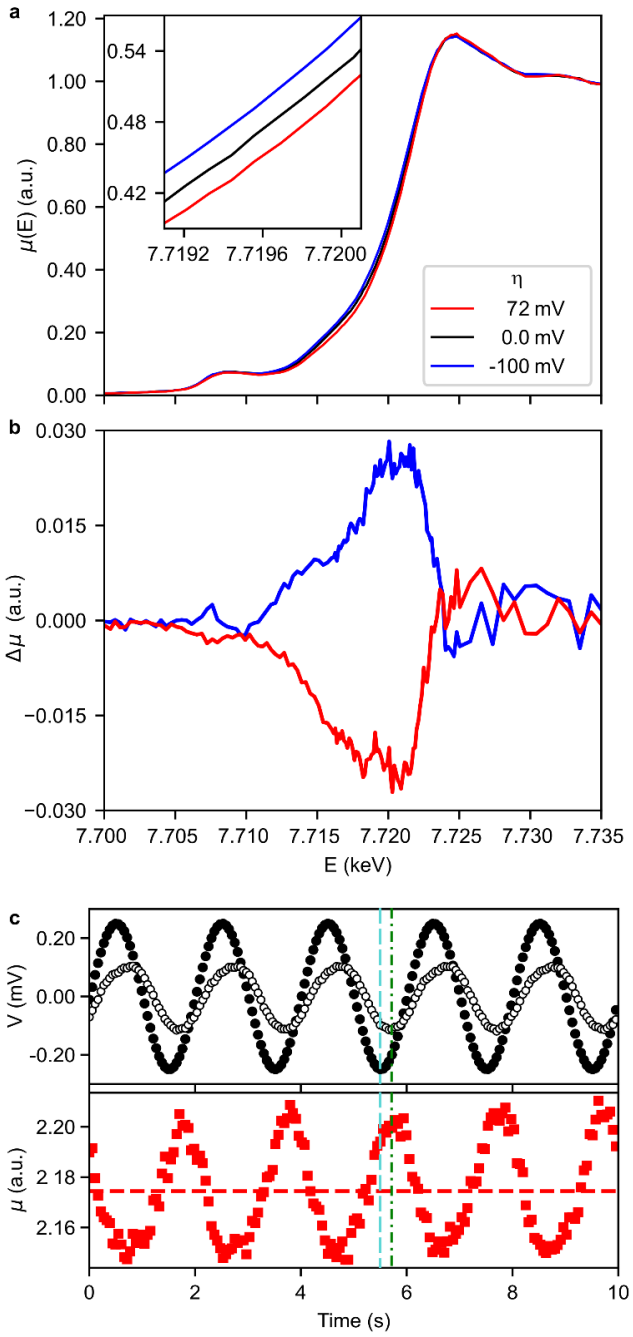

Figure 3.3. **a**, Co K-edge XANES spectra at 700 °C and a p_{O_2} of 0.10 bar under open cell voltage, anodic, and cathodic polarization. **b**, Difference spectra of absorbance in panel a with the open cell voltage spectrum as the reference. **c**, Time-domain waveforms of voltage (●), overpotential (o), and absorbance (■) for a 250 mV 0.5 Hz sinusoidal polarization. Vertical dashed cyan line and green dash-dotted lines indicate troughs of the voltage and overpotential signals, respectively. Horizontal red dashed line indicates the mean absorbance level.

electrode/electrolyte interface. The phase shift can be corrected during data analysis, but it is highly sensitive to R_Ω, which can be difficult to unambiguously determine, or may drift slightly during the measurement time. Alternatively, it can be accounted for during model formulation and interpretation, as we chose to do in this work.

Many factors influence the absolute magnitude of μ, but we most concerned with the vacancy concentration response to applied polarization.[28] Therefore, we focus on μ deviations by defining a displacement variable,

$$\Psi = \frac{\mu - \mu_o}{\mu_o} \tag{3.1}$$

where μ_o is the absorbance under equilibrium conditions. Vacancy concentration fluctuations are treated similarly by defining

$$\chi = \frac{x_v - x_v^o}{x_v^o} \tag{3.2}$$

where x_v is the oxygen vacancy mol fraction, and x_v^o is the equilibrium mol fraction for the measurement temperature and pO_2 conditions. We connect the two through $\Psi = \chi_o \chi$, assuming displacements are small enough that absorbance and vacancy concentration are linearly related and fully described by a single coefficient, χ_o.

Examining the in phase and out phase components of FR-XAS data is crucial for interpretation, much as it is with EIS. In other words, we want to determine the real and imaginary components of the absorbance signal from time-domain measurements at each position to produce one-dimensional (1D) images of oxygen vacancy profiles. In principle, 2D images with continuous spatial encoding can be produced by raster scanning the X-ray beam across an area of the patterned electrode, but those methodological improvements are the subject of future work. Analysis is performed using an open source Python package called frxas.py, and roughly follows the procedure in Ref. [48] for analyzing nonlinear EIS. Briefly, time-domain data are apodized by a Gaussian window function before applying a complex fast Fourier transform. Real and imaginary components of a signal at the oscillation frequency are extracted by fitting the resulting frequency spectrum. Absolute phase of each signal relative to the perturbation is established by finding the voltage phase angle $\varphi_1 = \tan^{-1}\frac{\mathrm{Im}}{\mathrm{Re}}$ and applying a first-order phase correction $\exp(-\mathrm{j}\varphi_1)$ to all

signals. Finally, FR-XAS profiles are generated by plotting the real and imaginary components of μ as a function of distance from the electrode gate.

3.6 RESULTS

Figure 3.4 shows FR-XAS profiles at 700 °C under several pO_2 for 150 mV amplitude voltage perturbations of various frequencies $\tilde{f}$. Profiles noted $\tilde{f}$ =0.00 Hz (steady state) were collected under DC polarization before FR-XAS measurements and are presented as one half of the difference between cathodically and anodically polarized profiles. We chose this representation for better comparison to oscillatory profiles, where the film experiences both cathodic and anodic polarization. At steady state, ψ is purely real (in phase) and decays exponentially away from the gate with a characteristic length reflecting the active region for ORR. At low oscillation frequencies (e.g. Fig. 3b, 0.25 Hz) $\mathrm{Re}[\psi]$ compresses slightly while $\mathrm{Im}[\psi]$ becomes nonzero thereby indicating a position-dependent phase shift in the vacancy concentration. At moderate and high frequencies (e.g. Fig. 3b, 1 and 5 Hz) $\mathrm{Re}[\psi]$ develops an inverted region following the initial decay, whereas $\mathrm{Im}[\psi]$ enlarges and the position of its minimum moves closer to the gate, demonstrating a diffusion limited profile corresponding to the Warburg impedance.[1,49] With increasing frequency, $\mathrm{Re}[\psi]$ and $\mathrm{Im}[\psi]$ at the gate decrease, which we attribute to the overpotential amplitude lowering from ohmic drop in the electrolyte. Furthermore, the active region decreases monotonically with increasing frequency, scaling approximately as $(1+2\pi\tilde{f})^{-1/2}$. To the best of the author's knowledge, Figure 3 shows the first direct measurements of concentration profiles during impedance measurements.

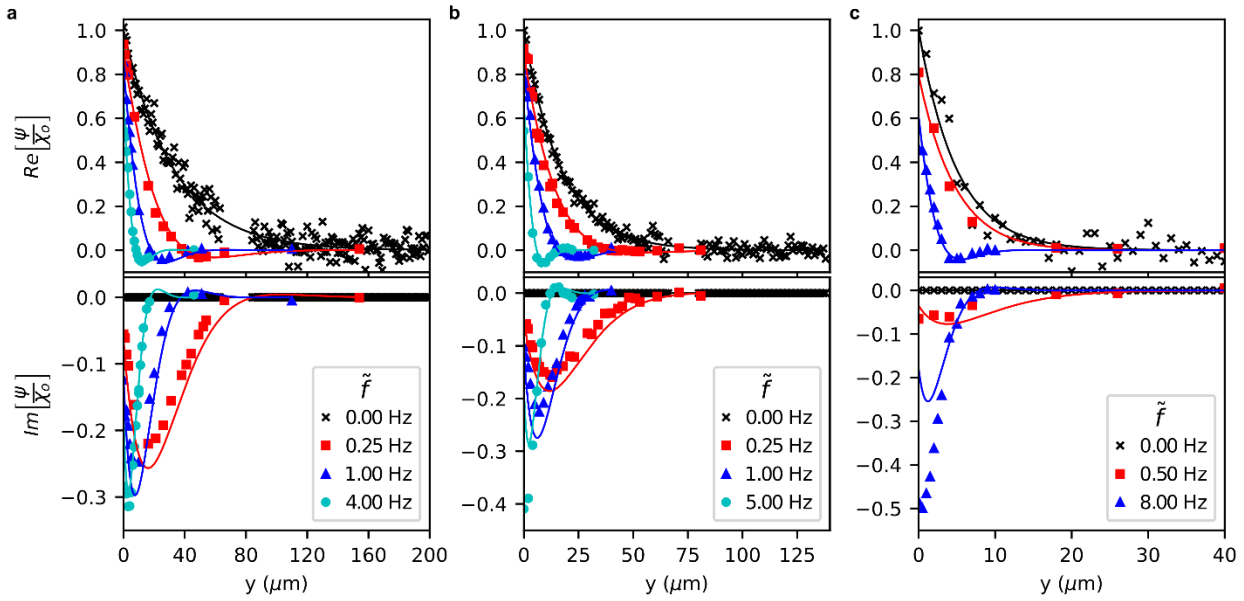

Figure 3.4 **a**, 0.01 bar. **b**, 0.10 bar. **c**, 1.00 bar. Steady state profiles before FR-XAS measurements using a separate fluorescence detector. Lines indicate best fit to equation (3.3). Profiles are normalized by χ_o, the empirical coefficient relating absorbance and oxygen vacancy displacements.

3.7 One-Dimensional Model and Discussion

Lines in Figure 3 are best fit results to a 1D model following a framework first proposed by Adler et al. for porous electrodes.[50] The model considers a dynamic material balance of oxygen vacancies in the mixed conductor with bulk transport of vacancies, and oxygen reduction on the surface $(\frac{1}{2}O_2 + 2e' + V_O^{\bullet\bullet} \rightleftharpoons O_O^X)$ treated as a homogeneous reaction within the 1D continuum. The electrolyte/electrode interface is assumed to be locally equilibrated where defect concentration is controlled by polarization, creating a driving force for oxygen exchange and vacancy diffusion propagating away from the interface. We assume oxygen transfer to the electrolyte only occurs at the gates and is blocked everywhere else by the insulating layer. The primary assumption of this 1D model is that vacancy gradients extend over distances much larger than the dimensions of microstructural features (i.e. electrode film thickness). The film thickness in this work is approximately L=600 nm, whereas vacancy gradients typically extend >10 μm (Figure 3.4).

Because the model is time dependent, we can predict vacancy profiles as functions in both time and space. However, under oscillating polarization the profiles are steady-periodic and the

position-dependent response can be isolated. For a voltage perturbation of frequency, the linearized, time-independent profiles are given by:

$$\chi = \frac{-1}{(1+\gamma\sqrt{1+j\tilde{\omega}t_G})} e^{-y/l_\delta\sqrt{1+j\tilde{\omega}t_G}} \tag{3.3}$$

where χ is the oxygen vacancy displacement from equilibrium, y is the distance from an electrode gate, l_δ is a characteristic length known as the utilization length, t_G is a characteristic time known as the Gerischer time constant, and γ is the ratio of electrolyte resistance to electrode resistance. The quantities l_δ and t_G are related to thermodynamic, transport, and kinetic properties by:

$$l_\delta = \sqrt{\frac{c_O D_v x_v^o}{4\Re_O^o}} \tag{3.4}$$

$$t_G = \frac{c_O x_v^o L}{4A_o\Re_O^o} \tag{3.5}$$

Where c_O is the molar concentration of oxygen lattice sites, x_v^o is the mole fraction of oxygen vacancies at equilibrium with the surrounding gas, $A_O = -1/2 \left.\frac{\partial \ln f_{O_2}}{\partial \ln x_v}\right|_{x_v = x_v^o}$ is the thermodynamic factor relating changes in composition to change changes in oxygen chemical potential via pO_2 or voltage, D_v is the oxygen vacancy diffusion coefficient, $\Re_O^o$ is the equilibrium molar exchange rate of O_2 between the MIEC surface and gas (as defined in Ref. [2] rather than a rate coefficient based on a particular rate law), and L is the thin film electrode thickness.

Examining the steady state limit of equation (3.3) reveals χ is purely real and decays exponentially over a distance l_δ. This reflects a response co-limited by diffusion and kinetics, where the size of l_δ is controlled by the relative rates of the two processes. At nonzero frequency, equation (3.3) suggests the profile should contract and develop a position-dependent imaginary component. At low frequencies ($1 > \tilde{\omega}t_G$, e.g. Figure 3.4c, 0.50 Hz) the profile is pseudo-exponential, suggesting lateral diffusion is fast enough to reestablish a quasi-steady profile as the defect concentration at the gate is modulated with AC polarization. With increasing frequency, the profile shortens, gains larger values of Im[χ], and develops a sign-inverted region of Re[χ] caused by polarization at the gate changing signs before the diffusion front fully propagates laterally into

the film. This indicates a transition from co-limited to diffusion-limited response, and occurs when $1 \approx \tilde{\omega} t_G$ (e.g. Figure 3.4b, 1 Hz). Finally, at high frequencies ($1 \ll \tilde{\omega} t_G$, e.g. Figure 3.4b, 5 Hz), the profile reduces to a purely diffusion-limited response corresponding to a Warburg impedance.[1,49] In the Warburg limit, we expect the profile to be independent of the surface exchange rate, allowing us to isolate and quantify the diffusion rate.

The denominator of equation (3.3) represents the impact of Ohmic drop in the electrolyte on the oxygen vacancy profiles in the electrode. Examining χ at the gate and in the absence of electrolyte resistance (γ=0), we expect χ will be purely real and unitary value. However, with nonzero γ, χ at the gate decreases in magnitude and adopts a finite imaginary component. As the frequency increases, the magnitude is further reduced and Im[χ] enlarges. These observations are attributed to impacts on the overpotential, which governs the vacancy concentration at the gate. With increasing frequency, the electrode impedance lessens relative to the electrolyte resistance, and a larger fraction of the cell voltage is consumed in the electrolyte. Therefore, the overpotential and χ magnitudes diminish. Moreover, the electrolyte resistance introduces a phase shift relative to the cell voltage, as illustrated by the definition of overpotential, $\eta = V - IR_\Omega$. Differences in the phase angles of voltage and current—often visualized as the imaginary component of impedance—influence the overpotential phase and, consequently, Im[χ] at the gate. FR-XAS profiles in Figure 3.4 support our interpretation about the influence of electrolyte resistance.

Model fits in Figure 3.4 generally agree quite well with the data; however, the model does not fully capture Im[χ] behavior. The 1 bar results show the least agreement, which may arise from gradient lengths approaching the gate width (~4 μm), therefore calling into question the 1D assumption. The model tends to overestimate Im[χ] at low and moderate frequencies, and underestimate at the highest frequencies. A possible explanation is the Al_2O_3 layer may not be perfectly insulating and allow small amounts of oxygen exchange outside the gate. We consider this below in the context of impedance measurements; however, a full explanation is the subject of ongoing work.

The parameters of best fit lines in Figure 3.4 are presented in Table 3.1. Absorbance data, ψ, is fit to equation (3.3) multiplied by the empirical coefficient, χ_o, to connect vacancy and absorbance displacements, as previously mentioned. χ_o is unique for each FR-XAS profile and,

whereas t_G and γ are shared between profiles within a pO_2. Values of l_δ are fixed during FR-XAS profile fitting and come from separately fitting the steady state profiles to an exponential decay with a baseline that is removed in Figure 3.4. Table 3.1 also includes vacancy diffusion and surface exchange rate coefficients calculated according to $D_v = \frac{1}{A_o}\left(\frac{l_\delta^{\,2}}{t_G}\right)$ and $\Re_O^o = \frac{1}{t_G}\left(\frac{c_O L x_v^o}{4A_o}\right)$, respectively. A_o and x_v^o values in Table 3.1 are estimated from impedance measurements at 700 °C over a wide range of pO_2 conditions on an LSC thin film sample using identical laser-deposition parameters, but without an insulating layer.

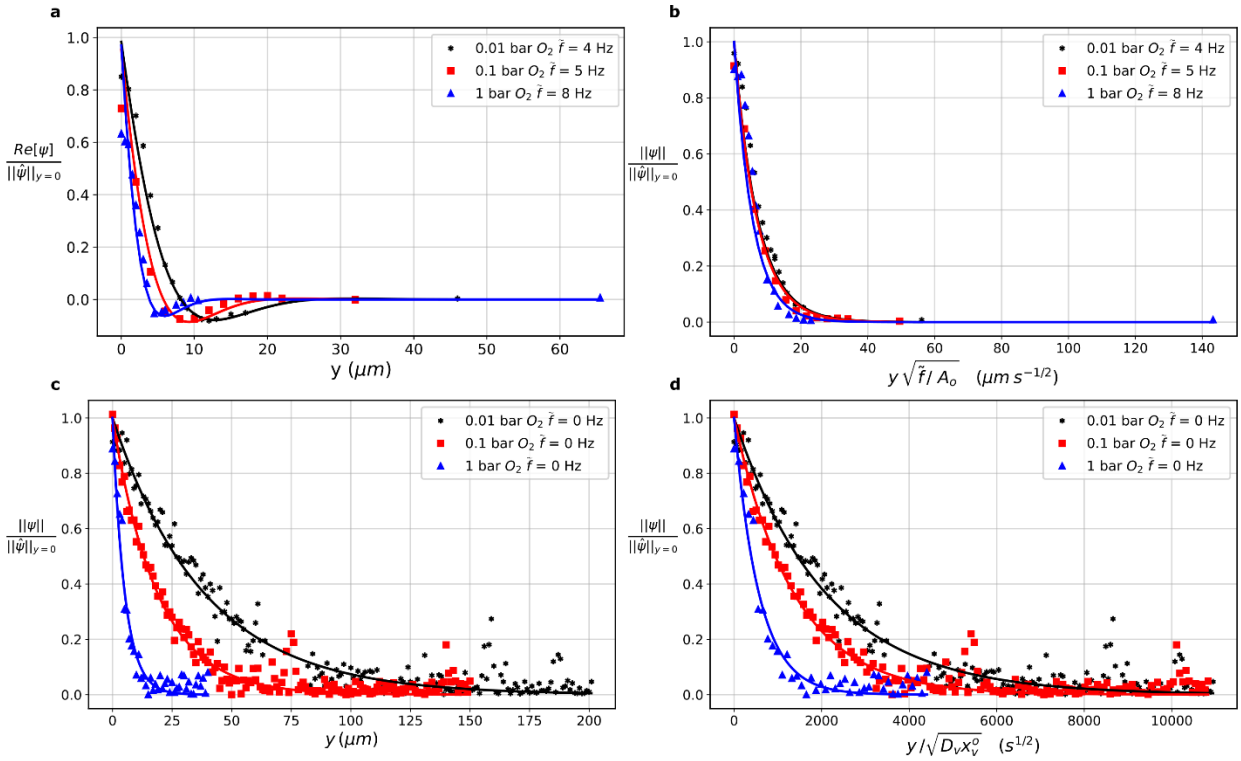

Figure 3.5 Select FR-XAS profiles: **a** Real component of the highest frequency at each pO_2 normalized to the magnitude at the gate edge and **b** with distance scaled to illustrate the D_v pO_2-dependence. **c,** Steady-state profiles at each pO_2 normalized to the magnitude at the gate edge and **d,** with distance scaled to illustrate the $\Re_O^o$ pO_2-dependence.

The best fit parameters in Table 3.1 show l_δ and t_G both decrease with pO_2, which agrees intuitively with contracting gradients and diminishing Im[χ] component of the lowest frequency FR-XAS profiles. D_v is only weakly pO_2-dependent, whereas $\Re_O^o$ varies by an order of magnitude over the measured conditions. These trends are further illustrated in Figure 3.5.

Figure 3.5a shows $\mathrm{Re}[\psi]$ normalized to the ψ magnitude at the gate edge for the highest frequency FR-XAS profiles under each pO_2, revealing the responses are self-similar and diffusionally-limited. We return to Eq. (3.3) to identify the transport rate scaling relationship with respect to pO_2. For simplicity, the discussion is presented in terms of χ, recalling ψ and χ are linearly related. We eliminate the electrolyte effect on $\mathrm{Im}[\chi]$ by examining the response magnitude, $\|\chi\| = \sqrt{\chi^* \chi}$. In the high-frequency limit, $\sqrt{1 + j\tilde{\omega} t_G} \approx \sqrt{j\tilde{\omega} t_G}$ and with the definitions of t_G and l_δ, Eq. (3.3) becomes:

$$\|\chi\| \sim e^{-y\sqrt{\frac{\tilde{\omega}}{2A_o D_v}}} = e^{-y\sqrt{\frac{\tilde{f}}{A_o}}\sqrt{\frac{\pi}{D_v}}} \tag{3.6}$$

Therefore, scaling distance by $\sqrt{\tilde{f}/A_o}$ reveals differences in the transport rate across the profiles, as illustrated in Figure 3.5b. All three scaled profiles are nearly identical, which implies D_v is only weakly sensitive to pO_2. Altogether, this analysis serves as visual justification for the trend seen in the best fit parameters.

Figure 3.5c presents stead-state $\|\psi\|$ profiles normalized by the value at the gate edge under each pO_2, showing exponential decays away from the gate where l_δ shrinks with increasing pO_2. Because D_v is approximately constant over this range, the contraction could be due to decreasing nonstoichiometry, increasing surface exchange rate, or both. We can isolate the cause by examining the magnitude of (3.3) in the steady-state limit:

$$\|\chi\| \sim e^{-\frac{y}{l_\delta}} = e^{-y\sqrt{\frac{1}{D_v x_v^o}}\sqrt{\frac{4\Re_O^o}{c_O L}}} \tag{3.7}$$

Therefore, scaling distance by $1/\sqrt{D_v x_v^o}$ accounts for nonstoichiometry changes, while any remaining dependence can be attributed to $\Re_O^o$ differences. Figure 3.5d shows that scaling the

distance reduces variations across the profiles, but a strong the remaining strong pO_2-dependence is caused by the surface exchange rate increasing. Moreover, $\Re_O^o$ appears to increase as $pO_2^{\sim 1/2}$. Again, this analysis provides visual evidence for the trend observed in the best fit parameters.

The noted trends in D_v and $\Re_O^o$ agree with previous work on porous LSC electrodes of the same composition; however, our values are approximately one order of magnitude higher and lower, respectively, than reported in literature.[2,51] Considering the confidence intervals on parameters here does not entirely account for the differences. Moreover, FR-XAS wields the benefit of directly probing the vacancy profiles, whereas previous works necessarily inferred kinetic and transport. Therefore, we are confident in the values reported here. Nonetheless, we propose possible sources of the discrepancy. First, unlike sintered particles in porous electrodes, thin films are formed from closely packed columns where boundaries between columns could exhibit different transport properties than the bulk material.[52,53] Next, surface exchange is highly sensitive to any amount of contamination or secondary phases, in addition to well-documented Sr-enrichment at the surfce.[54,55] In fact, the SEM image in Figure 3.1e shows bubble-like features and other debris of unknown composition decorated across the sample surface. We may speculate that such debris caused the apparently low surface exchange rates, but this remains an open question. Finally, simply exposing a PLD thin film to ambient air can change the exchange resistance by two orders of magnitude within the same sample.[45] Our reported parameters are certainly reasonable given these considerations for making direct comparison to bulk measurements.

3.8 Comparing to Measured Impedance

With the model presented above, we can predict the impedance response using parameters extracted from FR-XAS profiles. After neglecting ohmic resistance from the electrolyte bulk this produces a Gerischer impedance.

$$Z = \frac{R_G}{\sqrt{1 + j\tilde{\omega} t_G}} \tag{3.8}$$

$$R_G = \frac{RT}{8F^2} \frac{t_G A_o}{l_\delta c_O x_v^o LW} \tag{3.9}$$

where T is temperature, R is the ideal gas constant, F is Faraday's constant, and W is the sum of electrode gate lengths

Table 3.1. Utilization lengths and Gerischer time constants from best fits of equation (3.3) to profiles in Figure 3.4, including 95% confidence intervals from the regression analysis. Vacancy diffusion and equilibrium exchange rate coefficients are calculated using best fit parameter values. Equilibrium oxygen vacancy mol fractions and thermodynamic factors estimated from impedance measurements on a laser deposited LSC thin film at 700 °C under a wide range of p_{O_2}.

	p_{O_2}(bar)		
	0.01	0.10	1.00
l_δ (μm)	32.8 ± 1.03	17.1 ± 0.844	4.98 ± 0.589
t_G (s)	2.34 ± 0.168	0.946 ± 0.0891	0.145 ± 0.0314
D_v (cm^2/s)	1.70x10^{-6}	1.49x10^{-6}	1.02x10^{-6}
$\Re_O^\circ$ (mol/ cm^2 s)	4.47x10^{-9}	9.30x10^{-9}	4.36x10^{-8}
x_v^o	2.0x10^{-2}	1.3x10^{-2}	7.5x10^{-3}
A_o	2.70	2.09	1.67

Figure 3.6a shows impedance spectra of the patterned electrode at 700 °C before FR-XAS measurements along with predictions from equation (3.8) using parameters from Table 3.1. The measured impedance are depressed semicircular arcs with increased dispersion as pO_2 decreases and are not consistent with the expected Gerischer response in either shape or magnitude. The 45° tail at frequencies $\gg 1/t_G$ characteristic of diffusionally-limited response is notably absent from the measured impedance despite directly observing this behavior with FR-XAS. Furthermore, the predicted frequencies are approximately four times lower than measured. To bridge this gap, we propose an equivalent circuit model capturing additional contributions from other phenomena likely occurring in the patterned film. It is worth noting that any attempts to interpret kinetic or transport rates using impedance alone would be extremely challenging.

Figure 3.6b shows simulated impedance (dash-dot line) for the equivalent circuit model in panel c (open markers are the same data as in panel a), which includes phenomena likely occurring across the patterned electrode that contribute to the global response. Our relatively simple model, described in detail below, reflects the overall shape and magnitude of measurements better than

the 1-D model alone. Notably, the model captures a low-frequency tail appearing in the 0.10 and 1.0 bar measurements.

Two branches comprise the model after neglecting ohmic resistance attributed to ionic conduction through the electrolyte bulk. The bottom branch represents impedance from the mask layer and LSC film above the mask (Z_{NH}). The top branch includes a resistance preceding three parallel elements. The series resistance is caused by constriction effects (R_c) as current is funneled from the electrolyte superficial area into the narrow gate area. The first parallel element (Z_G) captures the Gerischer process imaged by FR-XAS and described above. The remaining two parallel elements (R_{gate} and C_{gate}) relate the surface reaction resistance and chemical capacitance, respectively, of LSC in the gate regions.

Impedance of the circuit model is calculated through a combination of predicted values and area-normalized measurements and presented in Table 3.2. We expect LSC in the gate regions may be treated as diffusionally equilibrated and rate-limited by surface kinetics, analogously to PLD films deposited directly onto an electrolyte. Following previous work on similarly prepared films,[3,5,26,56] the area specific resistance (ASR) from the oxygen reduction reaction, and volume specific capacitance (VSC) related to oxygen vacancy thermodynamics are described as:

$$\mathrm{ASR} = \frac{RT}{16F^2 \Re_O^o} \tag{3.10}$$

$$VSC = \frac{4F^2 c_O}{V_m \left(c_{fit} + \frac{RT}{\delta^o} \right)} \tag{3.11}$$

Where V_m is the molar volume ($33.7\ \frac{cm^3}{mol}$) and δ is the nonstoichiometry. The extensive quantities R_{gate} and C_{gate} are determined by applying the appropriate gate area and volume to ASR and VSC, respectively.

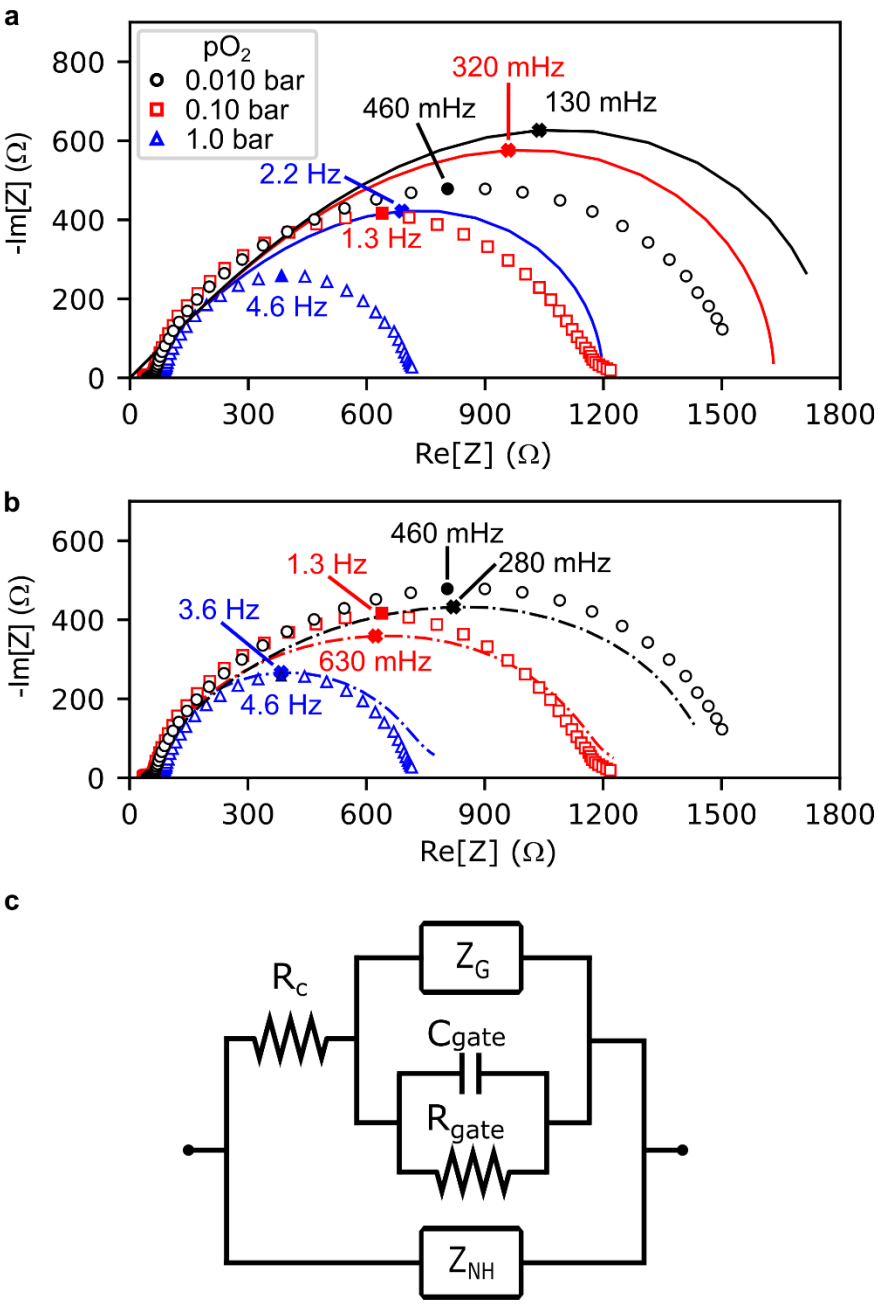

Figure 3.6 **a**, Measured impedance spectra at 700 °C after subtracting estimated electrolyte resistance (markers) compared to predicted Gerischer impedance (lines) using parameters in Table I. **b**, Measured impedance spectra (markers) compared to impedance predicted by the proposed equivalent circuit model. **c**, Proposed equivalent circuit model including contributions in parallel with the Gerischer impedance (Z_G): oxygen activity in the electrode above the gates (R_{gate}, C_{gate}), current constriction into the gates (R_c), and impedance of the insulating layer (Z_{NH}).

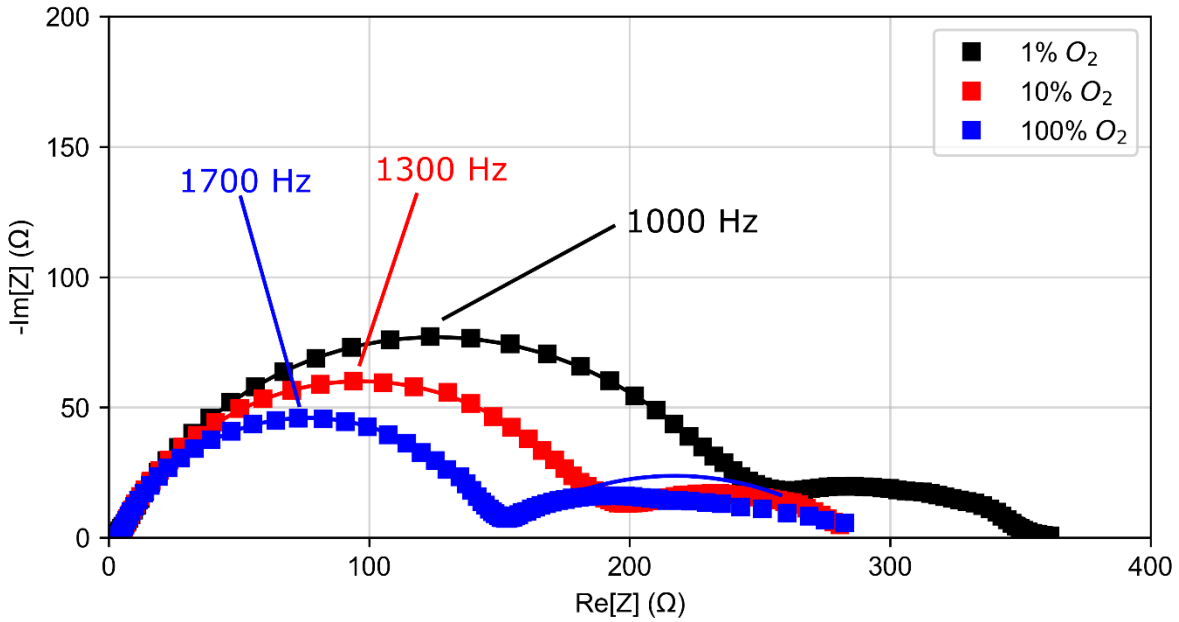

Figure 3.7 Impedance spectra at 700 °C of the "no hole" LSC sample after subtracting the high-frequency intercept.

Table 3.2. Circuit element values for the model proposed in Figure 3.6c.

pO_2 (bar)	0.01	0.1	1
R_c (Ω)	68	68	68
C_{gate} (F)	9.0×10^{-5}	7.5×10^{-5}	5.6×10^{-5}
R_{gate} (Ω)	26,000	13,000	2600
R_G (Ω)	1780	1630	1200
t_G (s)	2.34	0.946	0.145

We source Z_{NH} from impedance measurements shown in Figure 3.7, collected on an LSC film deposited onto the insulating layer without etching electrode gates to nominally force all current through the alumina layer. We refer to this sample as the "no hole" sample for the sake of brevity. The PLD conditions for fabricating the "no hole" sample were similar to those used for the patterned electrode samples; however, the superficial area and film thicknesses differed. The measured "no hole" data are scaled to the patterned electrode area in our circuit model, whereas an empirical fitting parameter is used to account for thickness differences, as discussed below.

We apply empirical scaling factors to each branch but shared across all three datasets. We find the values of both scaling factors with least-squares regression, yielding 2.1 for the top branch and 0.70 for the bottom branch. We chose this approach as a solution to the uncertainties associated with extrapolating our model to the full patterned electrode geometry. The top branch could be affected by inhomogeneous cation distributions, surface exchanges rates, and even film thickness variations. Sr-dopant in LSC is known to vary throughout a PLD film thickness but could also vary by lateral position,[3,5] potentially leading to distributed chemical capacitances and/or utilization lengths. Surface exchange rates, as previously noted, are strongly sensitive to any precipitated secondary phases or surface contamination, which we believe are present based on SEM images of the sample. Again, this inhomogeneous material property results in distributed surface exchange resistances and/or utilization lengths. Finally, nonuniform film thicknesses impacts C_{gate}, Z_G and Z_{NH} in both determining extensive quantities for each element and, potentially, modifying the underlying physical phenomena. For Z_G, thickness factors into the bulk vacancy diffusion rate. For $Z_{NH,}$ we used measurements from a sample where the insulating layer was two times thicker than in the patterned electrode. Without careful characterization, we speculate the contributing mechanism through this mask involves either ionic conduction through the alumina leading to low levels of additional oxygen exchange in LSC across the entire sample, or electronic conduction coupled to oxygen exchange at the mask/electrolyte interface. We cannot reasonably use a thickness adjustment for the mask impedance contribution in the patterned electrode without knowing the underlying physics involved. Regardless, we found that incorporating the "no hole" measurements into our model was necessary to reproduce the measured impedance magnitudes within ~50%.

Further investigations into the mask layer response are futile without further experiments; however, the gate region is partially responsible for non-Gerischer responses we observed. The top branch of our equivalent circuit model is a useful approximation for illustrating the interplay between the kinetically limited gate regions and co-limited gate-adjacent regions. However, this treatment is, by definition, not rigorous. In the following section, we present a model which captures the linear response of both components.

Despite achieving the success of our circuit model, the analysis emphasizes the challenge of unambiguously interpreting global measurements even with a model electrode. Although it is possible to conceive of our circuit model based on the impedance alone, it would be difficult to

draw strong conclusions about the material properties because the number of parameters involved could lead to large, accumulated errors. On the other hand, by directly quantifying the utilization length and assessing how the active region changes over the perturbation frequencies with FR-XAS we quantitatively capture both the ratio of kinetic and transport rates, and the timescale when transport becomes rate-limiting. The latter is measurable by impedance in an ideal system exhibiting a perfect Gerischer response; however, literature shows that is seldomly true.[2,4,34,57–62] Simultaneously quantifying the local length and timescales is the core feature distinguishing FR-XAS from other techniques used to study solid state electrochemistry.

3.9 Two-Dimensional Model and Discussion

The one-dimensional model presented above is a convenient framework to explain gross features of the measured impedance; however, at high frequencies we observe deviations from the 45° tail characterizing diffusion-limited behavior. This is one indication we cannot assume oxygen vacancies extend over length scales much greater than the film thickness. Furthermore, we cannot fully explain ψ variations at the gate edge with ohmic resistance from the electrolyte bulk alone. We suspect current constriction in the electrolyte near the gate regions leads to non-uniform potential distributions along the electrode/electrolyte interface. Therefore, we present a two-dimensional model including the gate regions and electrolyte. This model largely follows the treatment described by Cortney Kreller[4], but we restrict the development to the linear response assuming vacancy occurs solely via the bulk pathway and surface exchange is governed by a dissociative adsorption rate law.[63]

3.9.1 *Theory*

We adopt the Lankhorst model[64] for the oxygen vacancy thermodynamic behavior, which is described by the chemical potential of a neutral vacancy building unit, *v*, and its chemical potential are described in Equations (3.12) and (3.13), respectively.

$$v = \left\{ V_O^{\bullet\bullet} + 2e' - O_O^X \right\} \tag{3.12}$$

$$\mu_v = \mu_v^o(x) + RT\ln(x_v) + 2E_f(x_v) \tag{3.13}$$

Where $\mu_v^o(x)$ is the standard free energy of *v*, x_v is the bulk oxygen vacancy mole fraction, *x* is the Sr mole fraction, and $E_f(x_v)$ is the Fermi energy in relation to the value absent any oxygen nonstoichiometry. The thermodynamic factor, *A*, provides a relationship between changes in oxygen nonstoichiometry and chemical potential by the surrounding pO_2. When LSC is equilibrated with oxygen in the surrounding gas phase this becomes:

$$A_O = -\frac{1}{2}\frac{\partial \ln pO_2}{\partial \ln x_v} = 1 + \frac{b(x)x_v^o}{RT} \tag{3.14}$$

Where *b*(x) (~897 kJ mol^{-1} for this film[56]) is related the density of states at the Fermi energy.

We expect the vacancy concentration will be small compared to the oxygen lattice site concentration. Therefore, we expect vacancy diffusion to obey moderately dilute solution theory where gradients in chemical potential provide the driving force for diffusion.[65]

$$N_v = -\frac{D_v c_O}{RT}\nabla\mu_v = -D_v c_O\left(1 + \frac{bx_v}{RT}\right)\nabla x_v \tag{3.15}$$

Where D_v is the bulk vacancy diffusion coefficient, and c_o is the oxygen lattice site concentration.

Adler et al. first proposed a one-dimensional macrohomogeneous model for porous mixed conducting electrodes with high ionic conductivities.[50] The porous electrode microstructure was described by volume averaged properties of porosity, solid phase tortuosity, and surface area; however, the patterned electrode here has nominally well-defined geometry, no porosity, and unitary tortuosity. Therefore, we consider an oxygen vacancy material balance and substitute the bulk vacancy diffusion flux and thermodynamic factor definitions:

$$c_O\frac{\partial x_v}{\partial t} = -\nabla\cdot N_v = -\nabla\cdot\left(-D_v c_O\left(A_o + (A_o - 1)\frac{x_v - x_v^o}{x_v^o}\right)\nabla x_v\right) \tag{3.16}$$

We assume oxygen reduction at the surface is rate-limited by dissociative adsorption. The rate law, r_{O_2}, is then defined as:

$$r_{O_2} = k_o pO_2 x_v^2\left(1 - \left(\frac{x_v^o}{x_v}\right)^2 e^{-2\frac{b}{RT}\left(x_v - x_v^o\right)}\right) = \Re_O^o\left(\left(\frac{x_v}{x_v^o}\right)^2 - e^{-2\frac{b}{RT}\left(x_v - x_v^o\right)}\right) \tag{3.17}$$

Where k_o is the reaction rate constant for the dissociation step, and $\Re_O^o$ is the equilibrium surface exchange rate coefficient.[63]

We include the vacancy flux from the oxygen reduction reaction as a boundary conditions on the gas-exposed thin film surface:

$$N_v\big|_{x=L} = 2r_{O_2} \tag{3.18}$$

Where the x-axis is defined normal to the surface (to avoid confusion with nomenclature in the one-dimensional model), and L is the film thickness. We define another flux boundary condition at the electrode/electrolyte interface using Faraday's law to match the vacancy flux from the electrode to ionic current density in the electrolyte:

$$N_v\big|_{\substack{x=0 \\ 0<y<G}} = -\frac{i}{2F} \tag{3.19}$$

Where i is the current density and F is Faraday's constant. G is one half of the gate width because we consider an axisymmetric geometry centered around the gate midpoint. Therefore, no vacancy flux passes through the plane of symmetry:

$$N_v\big|_{y=0} = 0 \tag{3.20}$$

The gates are separated far enough apart that oxygen vacancies cannot transport between adjacent gates before being consumed by surface exchange. In other words, the film far away (~300 μm) from each is equilibrated with oxygen in the gas phase:

$$x_v\big|_{y\to\infty} = x_v^o \tag{3.21}$$

The electrode/electrolyte interface area of all gates combined is approximately three orders of magnitude smaller than the electrolyte superficial area. This interface will be influenced by current constriction effects caused by ionic current funneling into the gate regions. Therefore, we include the electrolyte to accurately capture the current distribution at the interface and the resulting vacancy flux into the electrode film. We include a large enough electrolyte domain such that potential gradients become perpendicular to the x-axis. We solve for the potential distribution in the electrolyte with:

$$\nabla^2\phi^{LT} = 0 \tag{3.22}$$

$$\nabla i = 0 \tag{3.23}$$

$$i = -\sigma_i \nabla\phi^{LT} \tag{3.24}$$

Where ϕ^{LT} is the potential in the electrolyte. Equation (3.22) is Laplace's equation, Equation (3.23) expresses the conservation of charge, and Equation (3.24) is Ohm's Law. We assume no ionic current passes from the electrolyte into the mask, and no vacancy passes from the electrode into the mask:

$$-\sigma_i \nabla \phi^{LT}\Big|_{\substack{x=0 \\ y\geq G}} = 0 \tag{3.25}$$

$$N_v\Big|_{\substack{x=0 \\ y\geq G}} = 0 \tag{3.26}$$

Ionic current leaving the electrolyte must equal the flux of neutral vacancy building units through the electrode/electrolyte interface. We relate the two by substituting Equation (3.19) into (3.24):

$$n \cdot (2FN_v) = n \cdot \sigma_i^{LT} \nabla \phi^{LT} \tag{3.27}$$

Where n is the normal vector aligned with the positive x-axis.

The cell voltage is defined by the Nernst equation relating oxygen fugacity in LSC to the oxygen partial pressure at the reference electrode:

$$\phi = \frac{RT}{4F} \ln\left[\frac{{f_{O_2}}^{MC}}{{pO_2}^{gas}}\right] \tag{3.28}$$

The mixed conductor electrode potential, ϕ^{MC}, and ϕ^{LT} are then defined as:

$$\phi^{LT} = \frac{\mu_{v_o}^{LT}}{2F} \tag{3.29}$$

$$\phi^{MC} = -\frac{\mu_{e^-}^{MC}}{F} \tag{3.30}$$

LSC with Sr dopant levels above ~0.1 exhibits a metallic band structure at temperatures above 500 °C with significantly higher electronic conductivity compared to the ionic conductivity.[51] Therefore, the potential will remain uniform throughout the electrode because the electron transference number is near unity. We define the current collector contacting the electrode

as the electrical ground, where the electrochemical potential of positively charged vacancies becomes:

$$\mu_{v_O} = -\frac{RT}{2}\ln\left[\frac{f_{O_2}}{pO_2}\right] + 2F\phi^{MC} = -\frac{RT}{2}\ln\left[\frac{f_{O_2}}{pO_2}\right] \tag{3.31}$$

Assuming local equilibrium at the electrode/electrolyte interface, the chemical potentials of the neutral vacancy unit are equal and we find the relationship for potential at this interface through Equations (3.29) and (3.31):

$$\phi^{LT} = -\frac{RT}{4F}\ln\left[\frac{f_{O_2}}{pO_2}\right] \tag{3.32}$$

We apply a sinusoidal voltage perturbation to the bottom edge of the electrolyte, which is considered our reference electrode. Cathodic voltage is positive from the reference electrode to the working electrode because we define the mixed conductor as our electrical ground. For a voltage perturbation of frequency $\tilde{\omega}$ and amplitude $\tilde{v}$:

$$\phi^{LT}\Big|_{x\to-\infty} = \tilde{v}\,\mathrm{Cos}(\tilde{\omega}t) \tag{3.33}$$

The model is nondimensionalized according to terms in Table 3.3 and linearized to give:

$$\frac{\partial\chi}{\partial\tau} = \nabla\cdot(\nabla\chi) \tag{3.34}$$

Where the dimensionless forms of the material balance boundary conditions in (3.18), (3.19), (3.20), (3.21), and (3.26) become:

$$n\cdot -A_o\nabla\chi\Big|_{\varsigma=1} = 2A_o\kappa \tag{3.35}$$

$$n\cdot A_o\nabla\chi\Big|_{\substack{\varsigma=0\\ 0<\xi<G/L}} = n\cdot -\gamma\nabla U \tag{3.36}$$

$$\nabla\chi\Big|_{\xi=0} = 0 \tag{3.37}$$

$$\chi\Big|_{\xi\to\infty} = 0 \tag{3.38}$$

$$\nabla\chi\Big|_{\substack{\varsigma=0\\ \xi\geq G/L}} = 0 \tag{3.39}$$

Where κ is a dimensionless parameter describing the relative roles of kinetics and bulk diffusion:

$$\kappa = \frac{2\Re_O^o L}{D_v c_O x_v^o} \equiv \frac{\text{surface exchange}}{\text{bulk diffusion}} \tag{3.40}$$

The dimensionless forms of the two remaining boundary conditions in the electrolyte given by (3.32) and (3.33) become:

$$U^{LT}\Big|_{\substack{\varsigma=0 \\ 0<\xi<G/L}} = A_o \chi \tag{3.41}$$

$$U^{LT}\Big|_{\varsigma\to-\infty} = \tilde{U}\,\mathrm{Cos}(\sigma\tau) \tag{3.42}$$

3.9.2 *Results & Discussion*

Figure 3.8a shows a portion of the simulated geometry simulated with the model described above highlighting details of the gate region, whereas Figure 3.9 shows the simulated vacancy displacement profiles in comparison to the measured values and one-dimensional model fits. The increased dimensionality yields only minor differences and tends to overestimate the imaginary component at moderate to low frequencies. The simulations agree better at higher frequencies, excellently matching the 4 Hz profile in 0.01 bar pO_2, and may suggest the measured imaginary values are anomalously low. Oxygen transport along the surface pathway is a possible, though unlikely, cause of the discrepancy. Effects from the mask layer or material property inhomogeneities are more likely, as discussed below.

Theoretically, any process in the mask involving oxygen would distort the phase relationship away from what is considered here. One possible scenario is the mask permits ionic current with a position-dependent phase due to current constriction effects near the gate. Distances further from the gate along the mask/electrolyte interface are more out of phase with respect to the

electrode/mask interface because the electrolyte potential experiences less funneling. Moreover, the chemical potential driving force for transport across the mask increases at those distances because the electrode is closer to equilibrium with the gas phase and the electrolyte is closer to the applied potential. Again, we can only speculate these effects without further characterizing the mask layer, yet we remain hopeful this discussion motivates additional studies.

Table 3.3. Patterned electrode and electrolyte model dimensionless parameters.

Quantity	**Dimensional Variable**	**Dimensionless Form**	**Dimensional Group**
Vacancies	x_v	$\chi = \frac{x_v - x_v^o}{x_v^o}$	x_v^o
Distance	x (Perpendicular to surface) y (Parallel to surface)	$\varsigma = x/L$ $\xi = y/L$	L ≡ Film Thickness
Time	t	$\tau = \frac{t}{t^*}$	$t^* = \frac{L^2}{A_o D_v}$
Frequency	$\tilde{\omega}$	$\sigma = \tilde{\omega} t^*$	$\frac{1}{t^*} = \frac{A_o D_v}{L^2}$
Voltage	V	$U = \frac{V}{V^*}$	$V = \frac{RT}{2F}$
Current	i	$\lambda = \frac{i}{i^*}$	$i^* = \frac{2Fc_O D_v x_v^o}{L}$
Conductivity	σ_i^{LT}	$\gamma = \frac{\sigma_i^{LT}}{\sigma_i^{MC}}$	σ_i^{MC}

The simulated impedance spectra shown in

Figure 3.8b more accurately reflect the measured high-frequency shape than with a one-dimensional Gerischer model alone. The surface plots at 10 Hz under 0.01 bar pO2 provide visual support that gradients within the gate region are at least partially responsible deviations away from 45° in the high-frequency tail. Surprisingly, minor gradients within the gate appear near the measured peak frequency at 0.40 Hz and could lead to slightly misidentifying the true peak frequency. That is, if these gradients always increase the apparent -Im[Z], the peak frequency shifts higher.

The low-frequency response, however, is similar to the one-dimensional model calculations. At these slower timescales, lateral gradients extend much further than the film thickness where the dimensional assumption is valid, and the gate contribution to the overall response is low. With the high-frequency response fully captured, the low-frequency response is evidently affected by something not measured with FR-XAS.

With extrapolating the impedance predicted from our local measurements we implicitly assume the imaged regions are representative of the entire sample; however, previous literature suggests otherwise. Cation composition varies throughout the film thickness, as characterized by TOF-SIMS, and workers proposed lateral inhomogeneities are also present in these films.[2,3,5] Moreover, SEM images of the film shown in Figure 3.1a expose debris and/or deposits present on the surface. We can only speculate about their origin and composition, but it stands to reason that such debris could alter surface kinetics nonuniformly, or at least physically obstruct gaseous access to the film. These theories are testable through extending FR-XAS imaging to two dimensions by rastering the X-ray beam across a sample area rather than measuring a pointwise line. In other words, the barriers are solvable technological, not fundamental, limitations.

We must step back to appreciate that we can raise these questions solely because the local concentration profiles were directly imaged. The issues raised here reemphasize how sensitive the electrochemical response in these materials is to every detail of the thermodynamics, transport,

and kinetic phenomena. We hope this motivates future workers to improve the technical implementation of FR-XAS and extend the frequency-resolved approach to other spectroscopies to address other previously intractable questions.

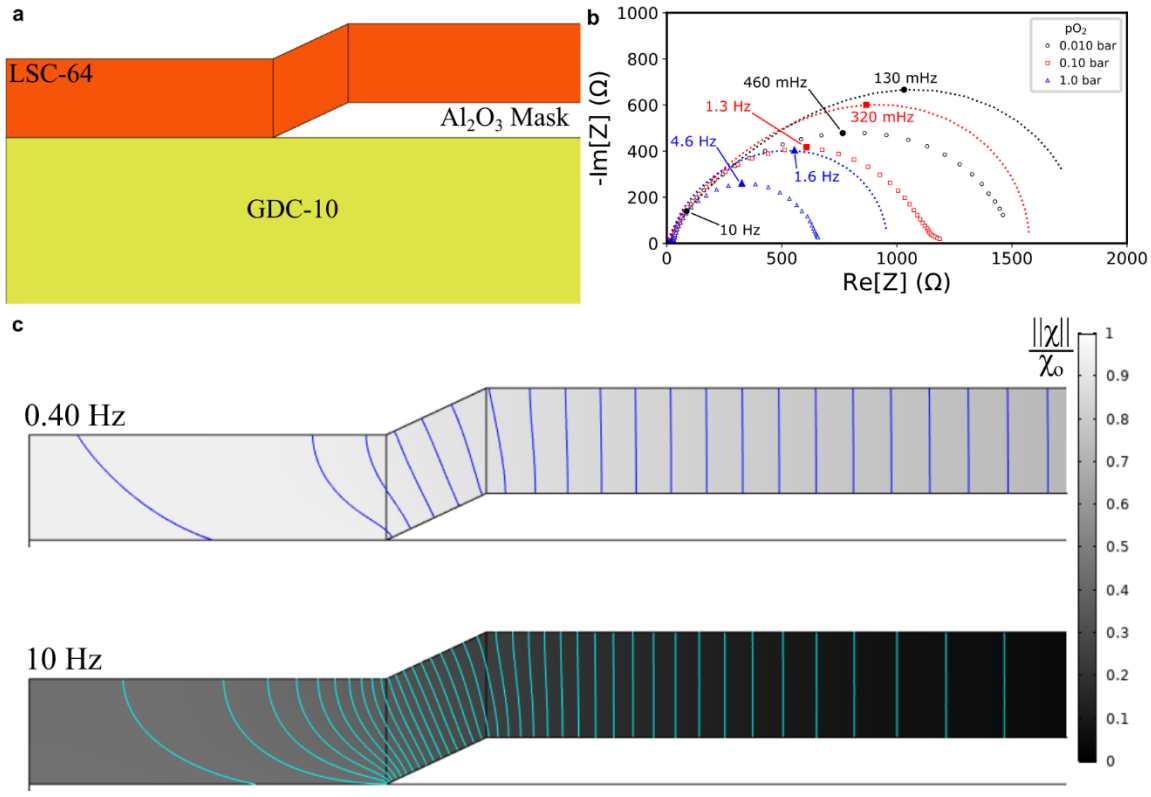

Figure 3.8 **a**, Patterned electrode geometry used in two-dimensional COMSOL simulations. **b,** Patterned electrode impedance measurements (markers) simulated impedance over the same frequency range. **c,** Surface plots overlaid with contours each representing 0.01 of normalized dimensionless vacancy concentrations under 0.01 bar pO_2.

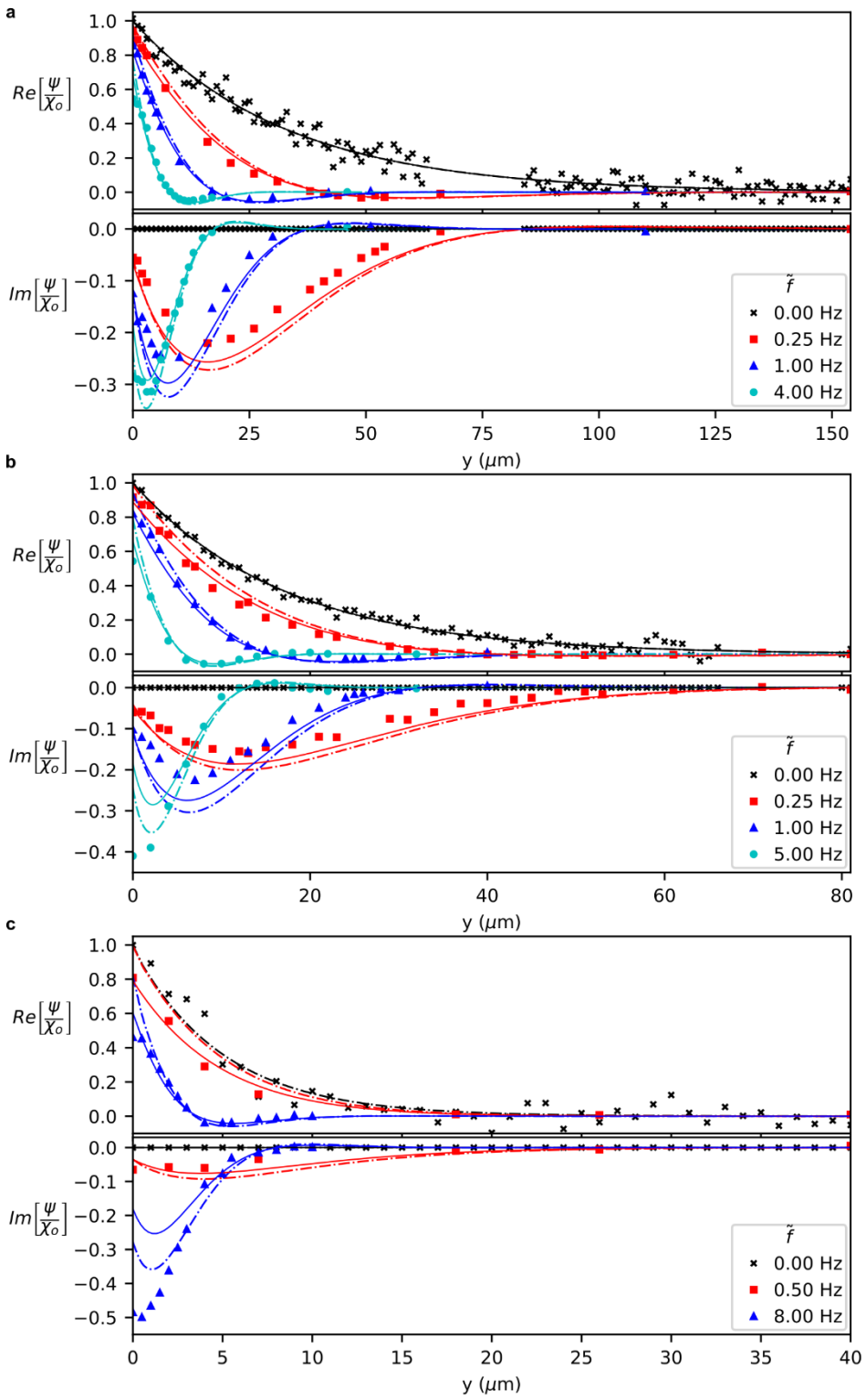

Figure 3.9 Normalized profiles of FR-XAS measurements (markers), one-dimensional predictions (solid lines), and two-dimensional simulations averaged over the x-axis (dash-dotted lines) under **a**, 0.01 bar **b,** 0.10 bar and **c**, 1.00 bar pO_2.

3.10 SUMMARY

We introduced frequency-resolved X-ray absorption spectroscopy and presented the first 1D images of concentration profiles associated with the Gerischer impedance. By analyzing these images with a 1D model, we extracted diffusion and kinetic parameters for the oxygen reduction reaction in a mixed ionic-electronic conducting cathode. Although the Gerischer alone does not match the measured impedance, we presented an equivalent circuit model showing greatly improved agreement by including contributions from the gate regions and mask layer. Finally, we developed a two-dimensional model to fully couple phenomena in the electrolyte and gate region with the imaged Gerischer response. Impedance simulations from this model successfully match the measured high-frequency response, yet quantitative agreement for the low frequencies remain an open question.

With the non-Gerischer processes occurring over similar timescales, quantitatively determining the material parameters would be challenging using global electrochemical techniques alone. This highlights the need for chemically sensitive, frequency-resolved techniques for gaining a deeper understanding of the chemical and physical phenomena governing materials used in electrochemical energy conversion. We hope this work motivates others to apply frequency-resolved approaches to other imaging modalities more suitable for studying material systems relevant in other electrochemical devices.

Chapter 4. DETECTING AND MANIPULATING THE SPACE CHARGE REGION IN ACCEPTOR-DOPED CERIA

The presence of a space charge region (SPR) at grain boundaries in ceria has been proposed to explain the p_{O2} dependence of the conductivity in nanocrystalline ceria for several decades, yet unambiguous measurements remain an actively researched topic.[12,17–19,66–68] This topic presents an excellent question to address with an SPM probe in conjunction with global measurements. Since ceria has long been studied as an SOFC electrolyte or SOEC electrode, there are extensive independent thermodynamic and material property measurements.[13,69–72] However, the nature of the SCR challenges the limits of SPM resolution since it is generally confined within 5 nm of the GB.[15–17,73] This is particularly challenging due to high topographic feature changes near the GB. Despite this, SPM offers advantages to locally probe defect chemistry in conjunction with global measurements.

4.1 SCANNING PROBE MICROSCOPY TECHNIQUES

The SPM techniques discussed herein are all based on atomic force microscopy (AFM) infrastructure. This distinction between AFM and SPM is made to distinguish SPM as probing functionalities in addition to topography.

4.1.1 *Resonance Enhancement*

Some SPM techniques require detection of displacements on the order of pm, which often falls below the detection noise floor. A commonly implemented remedy is oscillating the cantilever at the mechanical resonance frequency. This amplifies the response by two to three orders of magnitude. The response can then be interpreted by the damped harmonic oscillator model[74]

$$A(\omega) = \frac{A_i \omega_o^2}{\sqrt{\omega^2 \omega_o^2 / Q^2 + \left(\omega_o^2 - \omega^2\right)^2}} \tag{4.1}$$

$$\varphi(\omega) = \tan^{-1}\left[\frac{\omega \omega_o}{Q\left(\omega_o^2 - \omega^2\right)}\right] \tag{4.2}$$

Where A, A_i, and φ are the resonantly enhanced amplitude, the intrinsic amplitude, and relative phase of the response; ω_o, ω, and Q are the radial resonant frequency, radial applied frequency, and quality factor.

In practice, the mechanical resonance frequency is found by measuring a "tuning curve" where the frequency of the stimulus is swept through 10's of kHz. The stimulus can be mechanically driven through a piezo actuator, as is the case with tapping mode topography, electrical, as in piezoresponse force microscopy (PFM), or thermal, as will be discussed later. [75,76] This method is suitable whether the tip is in contact with a surface or not, provided the worker matches the appropriate interpretation for the relevant scenario.

A tuning curve calculated from Equations (4.1) and (4.2) is shown in Figure 4.1. Notable observations are amplification of the response by the quality factor, Q, at ω_o. At frequencies below ω_o, the phase is <90˚ indicating attractive forces dominate, whereas above ω_o, the phase is >90˚ indicating repulsive forces dominate. In practice, the cantilever is generally driven slightly off-resonance to avoid "phase switching", or changing between attractive and repulsive regimes, during a measurement scan. Phase switching often results in topographic artifacts that may impact the other functionalities probed by SPM.

4.1.2 *Strain-base Scanning Probe Microscopies*

Strain is common to every material system and is generally coupled with thermal, electrical or chemical phenomena. These couplings can be leveraged by SPM to study a multitude of material properties, leading to development of a class of SPM techniques called strain-based SPM (s-SPM). s-SPM techniques include piezoresponse force microscopy (PFM), electrochemical strain microscopy (ESM), and piezo-magnetic force microscopy (PmFM) [74].

An early example is piezoresponse force microscopy (PFM) in which an alternating voltage is applied to a conductive tip in contact with the surface of a piezoelectric or ferroelectric material. Through the converse piezoelectric effect, the voltage induces deformation, or strain, which is detected by the SPM tip. The amplitude and phase of the response relative to the voltage stimulus enables imaging of piezoelectric domains within the material.

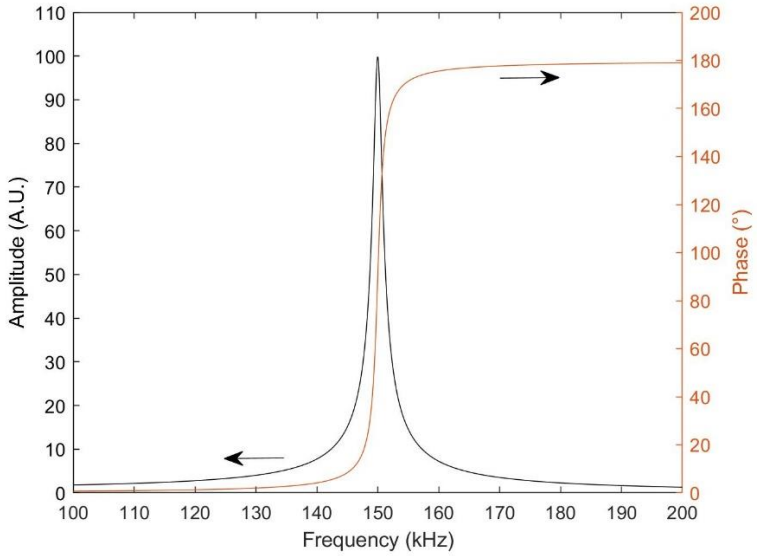

Figure 4.1 Resonance tuning curve for Ai=1, Q=100, and ωo=150 kHz with amplitude calculated by Eq. (4.1) and phase calculated by Eq. (4.2).

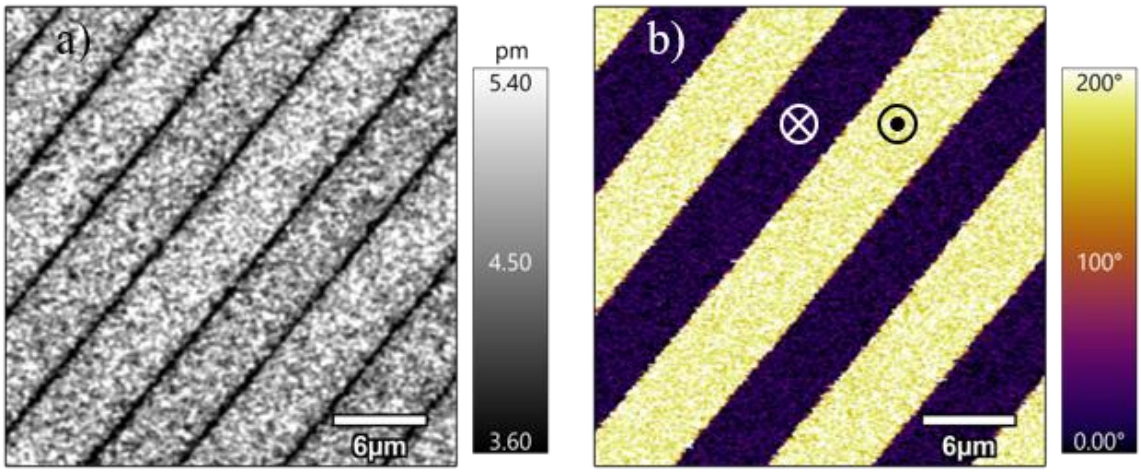

Figure 4.2 PFM a) amplitude and b) phase maps on PPLN reveal domain structure. The ⊙ and ⊗ symbols indicate upward and downward oriented domains, respectively. Figure reprinted with written permission of author. [77]

Figure 4.2 shows a PFM mapping of the model system periodically polarized $LiNbO_3$ (PPLN).[77] Areas with large amplitude response are associated with domain interiors, regardless of polarized direction, whereas regions of low amplitude indicate domain boundaries. The decrease in amplitude is caused by nullification of strain as the tip simultaneously excites oppositely polarized domains. Contrast in the phase map reveals domains based on different orientations of polarization. With a positive piezoelectric coefficient, a domain oriented upwards contracts when subjected to a positive potential, resulting in a 180˚ phase response. The converse is true for a domain oriented downwards.

Altogether, PFM is used here as an example to illustrate fundamental aspects of s-SPM. Namely, an oscillating stimulus is used to induce strain in a material that is resonantly enhanced to drastically improve signal-to-noise ratio. A complete study often involves repeating measurements parametrically with respect to temperature, AC voltage amplitude, or sample composition, interpreting the amplitude and phase of the strain response to elucidate the physics coupled to strain. This framework can be adapted based on the material system and physical phenomena to be probed.

4.1.3 *Scanning Thermo-ionic Microscopy*

Workers recently developed scanning therm-ionic microscopy (STIM), a new s-SPM technique employing thermal stress oscillations as the stimulus. [75,76] They were motivated in large part to develop a non-electric s-SPM to avoid excitation of undesirable electromechanical contributions that have hindered, to some degree, the utility of ESM. In principle, the electrically insulated nature of STIM allows nanoscale probing simultaneously with global electrochemical measurements.

At its core, STIM is believed to leverage Vegard strain, in which small deviations in solid ionic species are related linearly to lattice volume expansion. [78] This relationship therefore implies ionic species can be manipulated by applied stress, which has been independently observed in in Li intercalation materials and transition metal oxide perovskites. [79,80] In STIM the driving stress is applied as thermal stress induced by temperature gradients extending from a heated probe into the sample. Workers proposed a formalism for interpreting STIM response based on work by Larche and Cahn. [81]:

$$\Delta c(\omega t) = -\nabla \cdot \left[\frac{D\Omega}{RT_o} c_O \nabla \left(\frac{1}{3} t_r \left(\mathbf{C}\left(\boldsymbol{\varepsilon} - \alpha \Delta T(\omega t) \right) \mathbf{I} \right) \right) \right] \tag{4.3}$$

$$\Delta c(2\omega t) = -\nabla \cdot \left[\frac{D\Omega}{RT_o} c_O \Delta T(2\omega t) \nabla \left(\frac{1}{3} t_r \left(\mathbf{C}\left(\boldsymbol{\varepsilon} - \alpha \Delta T(2\omega t) \right) \mathbf{I} \right) \right) \right] \tag{4.4}$$

Where c, and T are concentration, and temperature; ω, and t are radial frequency, and time; D, **Ω**, α, and R are the diffusion coefficient, partial molar volume, thermal expansion coefficient, and ideal gas constant; **C**, **ε**, **I**, and t_r are the elastic stiffness tensor, total strain, second rank unit tensor, and trace of the matrix. A derivation of these equations can be found in Ref. [75].

In addition to the ionic concentration fluctuations at the first harmonic, ω, the analysis suggests a response at the second harmonic, 2ω, due to nonlinearity introduced by the 1/T. The first harmonic response is dominated by thermal stresses; however, the second harmonic response should occur solely due to ionic fluctuations since thermal expansion coefficients generally exhibit negligible nonlinearity. For simplicity, the first and second harmonic responses are referred to as "thermal response" and "ionic response," respectively. Tuning curves of the thermal and ionic response on ionically conductive ceria, and nonconductive PTFE, shown in Figure 4.3, suggest the principles of STIM are validate since both materials exhibit high thermal response, but only ceria exhibits significant ionic response.[76]

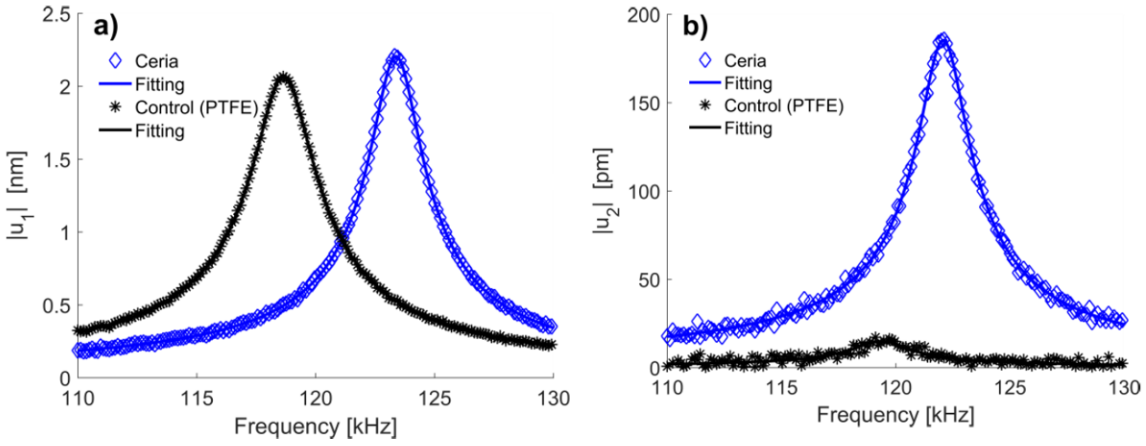

Figure 4.3. STIM a) thermal response and b) ionic response on ionically conductive ceria and nonconductive PTFE to validate STIM operating principles. Both materials exhibit a high thermal response, but the ionic response of PTFE is insignificant, as expected. Figure reprinted with written permission of author.[76]

4.1.4 *Sequential Excitation*

Due to the reliance on resonance enhancement for detecting s-SPM it is paramount to understand the degree of enhancement at each point in a measurement. However, the contact resonance frequency can shift dramatically even on nominally homogenous materials because of local changes in material stiffness, changes in tip-sample contact orientation, and other factors unrelated to local chemistry. Workers have addressed this problem with methods such as dual amplitude resonance tracking (DART), in which a frequency below resonance and a frequency above resonance are simultaneously applied. The amplitudes at each frequency are measured and a feedback loop is used to minimize the difference between the amplitudes by changing the applied frequencies.

Although DART is useful too, its implementation with STIM requires four lock-in amplifiers, and custom software to operate. Despite these challenges, workers have implemented DART-STIM on an AFM in China; however, this functionality is not yet operational at University of Washington. To circumvent this issue, workers proposed a technique called sequential excitation (SE) in which a series of single frequency mappings are recorded at the same physical are while parametrically sweeping through the excitation frequency. A schematic of the technique implementation and an example of the data contained within a single pixel are shown in Figure 4.4. The data is shaped into a three dimensional structure where $A(\omega,x,y)$, and the SHO model is fit to each pixel in post processing. This effectively allows resonance enhancement while including deeper information about the efficacy of the enhancement; however, SE is more computationally expensive, time intensive, and vulnerable to system instabilities, as will be discussed later.

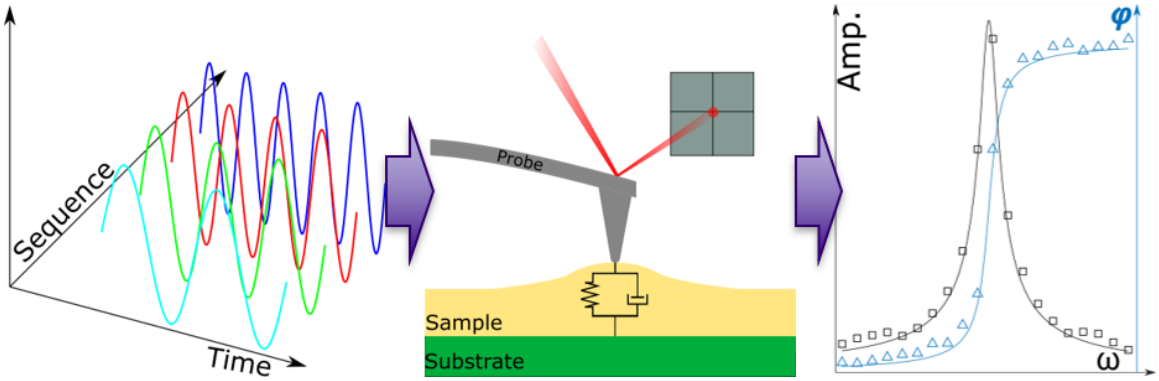

Figure 4.4. Schematic of SE implementation. An excitation parameter, shown here as frequency, is incremented along a sequence of SPM maps on the same physical area of the sample. The response at each sequence is ordered with respect to the incremented parameter and fit to a physically relevant model.

4.2 One-Dimensional Space Charge Region Model

SCRs appear near electrically charged interfaces in solids as a mechanism for charge compensation and are conceptually comparable to the double layer found near electrodes in aqueous electrolytes. In pure and acceptor-doped ceria, the grain boundary core accumulates positive charge, likely due to vacancy segregation in the former and dopant segregation in the latter.[82–84] The charge is compensated on both sides of the GB core by a depletion of vacancies and an accumulation of electrons. Vacancy depletion is believed to cause the poor ionic conductivity attributed to grain interfaces in the brick layer model.[66] Furthermore, as the grain size approaches the length scale of the SCR the accumulation/depletion profiles begin to overlap, and the grain interiors behave less like bulk ceria.

The potential distribution in the SCR is calculated using the Poisson equation solved assuming the charge density is dominated by an immobile charge carrier, i.e. dopant atom:

$$\phi = -\frac{z_{IM} c_{IM} e}{2\varepsilon_r \varepsilon_o}\left(x - \lambda^*\right)^2 ; x < \lambda^* \tag{4.5}$$

$$\lambda^* = \sqrt{-\frac{2\varepsilon_r \varepsilon_o \phi_o}{z_{IM} c_{IM} e}} \tag{4.6}$$

Where ϕ, and ϕ_o are electric potential, and electric potential at the GB core; e, k_b, ε_r, and ε_o are elementary charge, Boltzmann constant, relative permittivity, and permittivity of vacuum; z_{IM} and c_{IM} are the charge number and bulk concentration of the immobile charge carrier.

The concentration profiles of the mobile charged species are then calculated by the Boltzmann equation:

$$c_i = c_{i,\infty} \cdot e^{\frac{-z_i e}{k_b T}\phi} \tag{4.7}$$

Where c_i, $c_{i,\infty}$, and z_i are the concentration, bulk concentration and charge number of a mobile carrier in the SCR[15]. Concentration profiles in Figure 4.5 were calculated assuming a value of +0.3 V for ϕ_o in the unbiased state, and +0.5 V in the biased state to capture the application of a +0.2 V per grain bias. The calculations in the biased state illustrate anticipated increased accumulation of polarons on one side of the GB concomitant with decreased accumulation of polarons on the opposite side of the GB. Furthermore, the SCR is expected to extend on one side of the GB and contract on the other.

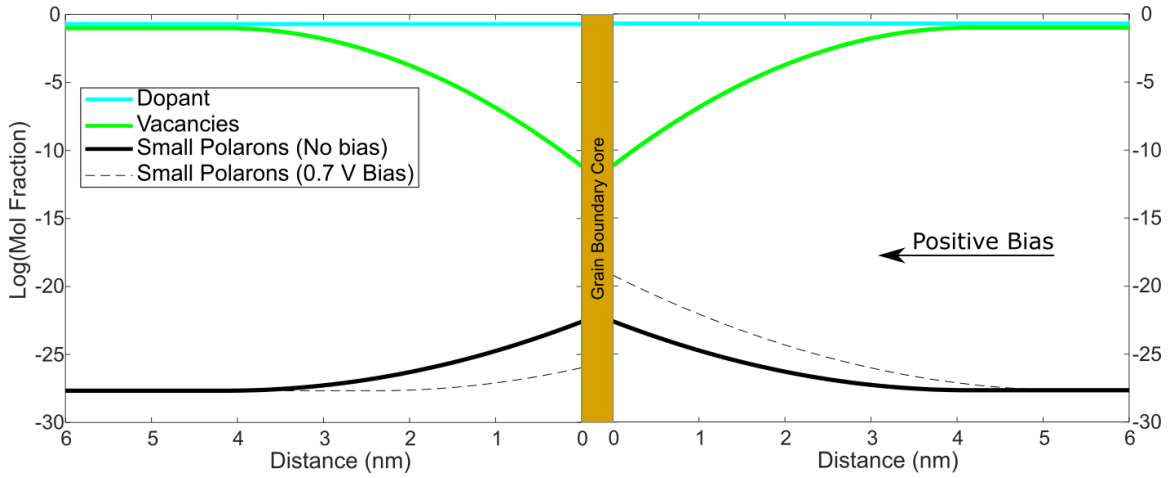

Figure 4.5. Calculated concentration profiles of SPR assuming flat dopant profile and vacancies immobile at 25˚ C in air.

4.3 Sample Fabrication

Approximately 1.5 g of 10 mol% Gd-doped CeO_2 (GDC-10, Fuel Cell Materials) with an estimated average grain size of 2 μm was uniaxially pressed in a 13 mm diameter die at 10,000 psi for 3 minutes, then fired at 1300 °C for 4 hours, ramping at 2 °C/ min. One side of the pellet was planarized with 30 μm SiC sand paper before polishing with 5 μm, 1 μm, and 0.25 μm diamond slurry on a rotary polishing machine. The pellet was re-fired using the previous sintering protocol to calcine any remaining polishing media and reestablish grain structure. Gold electrodes were deposited on the polished surface using a sputter coater and a steel mask. The mask was patterned to allow deposition of two semicircle electrodes 5 mm in radius with approximately 100 μm separating the straight edge of the semicircles. The separation distance was chosen to achieve approximately 0.2 V per grain when applying the maximum 10 V by the AFM electronics.

All experiments were performed on an Asylum Reseach Cypher atomic force microscope using an ElectriTap190-G with a spring constant around 15 N/m. The probe was heated with blueDrive photothermal excitation functionality of the Cypher to apply temperature stimulus. An atmosphere of 20% O_2 balance N_2 was maintained in the sample chamber to avoid transient surface chemistry due to humidity, volatile organics, or reduction of the ceria itself. To avoid thermal drift of the AFM piezomotors a thermalization period of at least three hours was observed upon introducing the sample to Cypher, and following temperature changes.

4.4 Results & Discussion

Figure 4.6 shows maps of the fit ionic response A_i values in the unbiased state and under application of (+)/(-) 0.2 V/ grain at 120 °C and 30 °C. In Figure 4.6 a), increased response on the left side of grains II and V, and decreased response on the right side of grains I and IV agrees with expectations for a positive bias. The opposite effect is seen upon inverting polarity of the bias. With no bias, the response is enhanced symmetrically around grain boundaries. These observations may be easily overemphasized, however, given the SPR length is 5-10 nm, corresponding to 1-2 pixels. Additionally, the probed volume beneath the probe has not been well characterized for STIM, therefore it is unknown whether the response apparently extending 10's nm from the GB is physically significant. Despite these concerns, the apparent trends are promising.

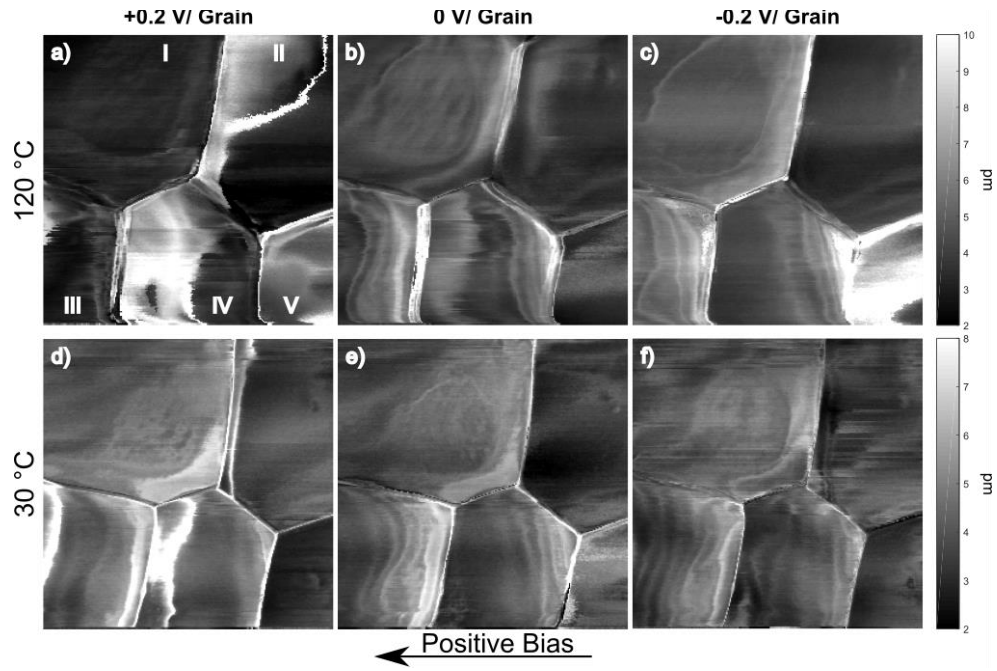

Figure 4.6. Maps of ionic response fit A_i at (a-c) 120 °C and (d-f) 30 °C under (a,d) +0.2 V/ grain, (b,e) 0 V/ grain, and (c,f) -0.2 V/ grain. Images are 1.5 μm x 1.5 μm.

Enhanced response near GBs appears broadened at 120 °C, though this effect is most notable with no applied bias. Furthermore, ionic response within grains is larger at higher temperatures implying larger populations and/or increased mobility of ionic species. The former interpretation is supported to some degree by the n-type semiconducting properties of GDC. More analysis of heat transport during STIM measurements is relevant to clarifying this interpretation as the increased sample temperature in conjunction with the average probe temperature could activate oxygen vacancy transport, which has been neglected so far.

In general, GBs exhibit larger responses consistent with previous SPM measurements, though GB parallel to the fast scanning direction (left to right) notably deviate from this behavior. Contrarily, the enhanced response at the GB between II and V suggests the poor response between I and III could be due to differing local transport properties. The crystallographic nature of these GB may influence the transport properties as surface energetics are heavily influenced by atomic arrangement. Without crystallographic information identifying the nature of these GBs, these observations remain speculative.

The R^2 values corresponding to the A_i maps in are shown in Figure 4.7. Fits are robust for much of the scanned area, and for grain interiors in particular; however, the GB fits are troublingly poor. The cause of poor fitting is not clear, though it could arise from one or more contributing effects. At GBs, the topographic change is most pronounced and could lead to the probe tip probing both adjacent grains simultaneously. In this case, the damped harmonic oscillator model does not capture the physical scenario. A new model to capture these physics might be proposed, potentially with two damped harmonic oscillators in parallel; however, implementation of such a protocol would be challenging as this model would be selectively applied to certain pixels in a map. Furthermore, the distance away from a GB where this model applies is ambiguous, leading to a significant possibility of applying the new model to regions that should behave as single damped harmonic oscillators.

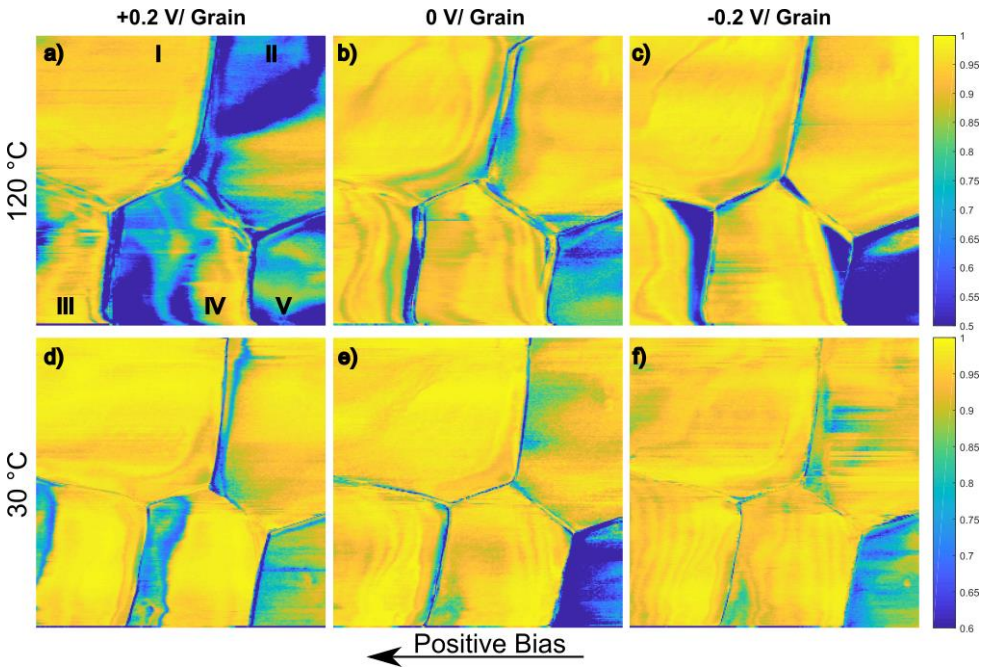

Figure 4.7. Maps of R^2 values for ionic response fits at (a-c) 120 °C and (d-f) 30 °C under (a,d) +0.2 V/ grain, (b,e) 0 V/ grain, and (c,f) -0.2 V/ grain. Images are 1.5 μm x 1.5 μm.

Another possibility is "pixel drift", in which the location of a GB alternates between several adjacent pixels due to some failure in post processing. Since the SPR is expected to only extend over 1-2 pixels, the response in this area is highly sensitive to drift in the imaging area. This is a likely scenario as the many images used for a single SE map are aligned through a cross-correlation algorithm that may not be powerful enough to account for drift at scales this small. Temperature

gradients in AFM piezomotors that are unstable over the duration of an SE experiment could also contribute since the distance covered by a single pixel could change between scans. The extent to which this effected contributed is difficult to quantify without complimentary imaging on the same region to verify sample geometry.

Several features of the response are likely artifacts of post processing. The streak of high response in grain II and the overall high response of grain IV in Figure 4.6 a) are associated with poor R^2 values in Figure 4.7 a), and are unique to that set of conditions. A similar pattern of response should appear in the other maps if the response were physically significant. Grains IV and V in d) and c), respectively, also exhibit suspicious response and are associated with lackluster R^2 values. Intuitive explanations for these failures are not clear as was the case for features near GB, therefore suggesting SE may not bet particularly robust for achieving resonantly enhanced s-SPM measurements. On the other hand, modifying experimental details, such as decreased scan area, high aspect ratio probe, and longer thermalization times, could yield more successful measurements.

4.5 SUMMARY

SE-STIM was measured at 30 °C and 120 °C under +0.2, 0, and -0.2 V/grain applied bias on a GDC pellet. The ionic response between grains I and II at 120 °C appear qualitatively consistent with expectations from a 1D Mott-Schottky model; however, these observations are not consistent at all grain boundaries. Furthermore, several maps contain areas of high response within grains that are likely artifacts of post processing based on the correspondingly low R^2 values in those regions. Many GB responses are also associated with poor R^2, though the origin of these model failures is unclear. Although these issues may be mitigated by several experimental considerations, the confined nature of the SPR and large topographic changes at GB challenge the limits of SPM.

Chapter 5. SUMMARY AND RECOMMENDATIONS

The primary objective of this work was developing new techniques to directly measure processes in electrochemical materials so the broader scientific community can more quickly understand fundamental rates and limitations. We explored both MIEC cathode and ceramic electrolyte materials as systems where chemically-sensitive spatiotemporal measurements could solve open questions about performance-limiting phenomena.

5.1 Strain-based Scanning Probe Microscopy

We discussed strain-based scanning probe methods for imaging local ionic concentrations and highlight STIM, the technique developed by collaborators in the Department of Mechanical Engineering here the University of Washington. We used STIM to investigate SPRs at GDC grain boundaries. We produced encouraging results suggesting we imaged SPRs and manipulated their orientation with DC polarization. However, we are skeptical of the results because of inconsistent grain boundary responses and apparent topographical influences.

Although our efforts on this project ended without a satisfying conclusion, we expect a different material system, or simplified geometry in ceria would be more successful. With further literature review, we realized SPRs are minimized in the GDC composition studied here. In contrast, ultrapure ceria experiences larger SPR effects associated with longer, more detectable length scales. Furthermore, seeking collaborators to synthesize ceria bicrystals, or another morphology with well defined interfaces would eliminate topographical influences. A simplified model system such as this is necessary to fully validate the working principles of STIM.

5.2 Dynamic X-ray Spectroscopy & FR-XAS

We used dense thin film LSC electrodes to demonstrate that XAS could probe vacancy concentrations at critical timescales and under relevant SOFC conditions. The most significant products of this validation step were the software programs for data acquisition and analysis subsequently applied in FR-XAS. Beyond that, dynamic XANES spectra confirmed that Co K-edge absorption shifts were maximized at the peak frequencies identified in EIS, whereas near the high frequency intercept only mild shifts were seen. We interpretted the XAFS from these

measurements, but the energy range and resolution prevented definitive conclusions. Regardless, we achieved the primary goal in this preliminary validation step.

Next, we applied FR-XAS to a patterned electrode designed to create large vacancy gradients extending laterally away from defined electrode/electrolyte contact areas. We produced, to the best of our knowledge, that first direct measurements of concentration profiles originally predicted by Heinz Gerischer in 1951. We extracted transport and surface exchange properties from the one-dimensional images that agreed with pO_2-dependence in previous literature reports. Although our model qualitatively explained the data, we relied on empirical amplitude factors to compare with stead-state measurements, and could not establish absolute vacancy concentrations. Furthermore, the measure impedance was not consistent with our model predctions. We attributed this to ionic current leaking through the insulating mask, and proposed a simple circuit model that captured both the impedance shape and frequency response.

We propose extending FR-XAS measurements into two-dimensional images by rastering the X-ray beam across the sample surface in the same way SPM images are collected. This would reveal any variations in the transport and surface exchange rates across the sample that could arise from nonuniform electrode thickness or debris blocking access to the surface. If this were the case, we expect a distribution of ORR timescales resulting in distorted impedance. In fact, we achieved the first step towards 2-D images by collecting FR-XAS while continuously scanning the position. Furthermore, we implemented this improvement with the fluorescence detector used in steady-state measurements to address concernts about the absolute vacancy concentrations. Unfortunately, complications with samples limited our measurements to a single pO_2 and prevented reasonable comparison to the results presented in Chapter 3. Furthermore, the COVID-19 pandemic prevented a final trip to SPring-8 synchrotron facility after we implemented the technical advancements described above.

BIBLIOGRAPHY

(1) Adler, S. B. Factors Governing Oxygen Reduction in Solid Oxide Fuel Cell Cathodes. *Chem. Rev.* **2004**, *104* (10), 4791–4844. https://doi.org/10.1021/cr020724o.

(2) Lu, Y.; Kreller, C.; Adler, S. B. Measurement and Modeling of the Impedance Characteristics of Porous La1 − x Sr x CoO3 − δ Electrodes. *J. Electrochem. Soc.* **2009**, *156* (4), B513–B525. https://doi.org/10.1149/1.3079337.

(3) Kreller, C. R.; McDonald, T. J.; Adler, S. B.; Crumlin, E. J.; Mutoro, E.; Ahn, S. J.; O', G. J. la; Shao-Horn, Y.; Biegalski, M. D.; Christen, H. M.; Chater, R. R.; Kilner, J. A. Origin of Enhanced Chemical Capacitance in La0.8Sr0.2CoO3-δ Thin Film Electrodes. *J. Electrochem. Soc.* **2013**, *160* (9), F931–F942. https://doi.org/10.1149/2.021309jes.

(4) Kreller, C. R. Measurement and Modeling of Material and Microstructural Factors Governing Performance of Solid Oxide Fuel Cell Cathodes. Ph.D., University of Washington, United States -- Washington, 2011.

(5) McDonald, T. J. Characterization and Modeling of La1-XSrxCoO3-Delta Solid Oxide Fuel Cell Cathodes Using Nonlinear Electrochemical Impedance Techniques. Ph.D., University of Washington, United States -- Washington, 2014.

(6) Kilner, J. A.; Burriel, M. Materials for Intermediate-Temperature Solid-Oxide Fuel Cells. *Annual Review of Materials Research* **2014**, *44* (1), 365–393. https://doi.org/10.1146/annurev-matsci-070813-113426.

(7) Jacobson, A. J. Materials for Solid Oxide Fuel Cells. *Chem. Mater.* **2010**, *22* (3), 660–674. https://doi.org/10.1021/cm902640j.

(8) Steele, B. C. H. Appraisal of Ce1−yGdyO2−y/2 Electrolytes for IT-SOFC Operation at 500°C. *Solid State Ionics* **2000**, *129* (1), 95–110. https://doi.org/10.1016/S0167-2738(99)00319-7.

(9) Wang, S.; Kobayashi, T.; Dokiya, M.; Hashimoto, T. Electrical and Ionic Conductivity of Gd-Doped Ceria. *J. Electrochem. Soc.* **2000**, *147* (10), 3606–3609. https://doi.org/10.1149/1.1393946.

(10) Inaba, H.; Tagawa, H. Ceria-Based Solid Electrolytes. *Solid State Ionics* **1996**, *83* (1), 1–16. https://doi.org/10.1016/0167-2738(95)00229-4.

(11) Mogensen, M.; Sammes, N. M.; Tompsett, G. A. Physical, Chemical and Electrochemical Properties of Pure and Doped Ceria. *Solid State Ionics* **2000**, *129* (1–4), 63–94. https://doi.org/10.1016/S0167-2738(99)00318-5.

(12) Kim, S.; Maier, J. On the Conductivity Mechanism of Nanocrystalline Ceria. *J. Electrochem. Soc.* **2002**, *149* (10), J73–J83. https://doi.org/10.1149/1.1507597.

(13) Chiang, Y. -M.; Lavik, E. B.; Kosacki, I.; Tuller, H. L.; Ying, J. Y. Defect and Transport Properties of Nanocrystalline CeO2−x. *Appl. Phys. Lett.* **1996**, *69* (2), 185–187. https://doi.org/10.1063/1.117366.

(14) Christie, G. M.; van Berkel, F. P. F. Microstructure — Ionic Conductivity Relationships in Ceria-Gadolinia Electrolytes. *Solid State Ionics* **1996**, *83* (1), 17–27. https://doi.org/10.1016/0167-2738(95)00155-7.

(15) Göbel, M. C.; Gregori, G.; Maier, J. Numerical Calculations of Space Charge Layer Effects in Nanocrystalline Ceria. Part II: Detailed Analysis of the Space Charge Layer Properties. *Phys. Chem. Chem. Phys.* **2014**, *16* (21), 10175–10186. https://doi.org/10.1039/C3CP54616K.

(16) Göbel, M. C.; Gregori, G.; Maier, J. Numerical Calculations of Space Charge Layer Effects in Nanocrystalline Ceria. Part I: Comparison with the Analytical Models and Derivation of Improved Analytical Solutions. *Phys. Chem. Chem. Phys.* **2014**, *16* (21), 10214–10231. https://doi.org/10.1039/C3CP54615B.
(17) Tschöpe, A.; Sommer, E.; Birringer, R. Grain Size-Dependent Electrical Conductivity of Polycrystalline Cerium Oxide. *Solid State Ionics* **2001**, *139* (3), 255–265. https://doi.org/10.1016/S0167-2738(01)00678-6.
(18) Tschöpe, A. Grain Size-Dependent Electrical Conductivity of Polycrystalline Cerium Oxide II: Space Charge Model. *Solid State Ionics* **2001**, *139* (3), 267–280. https://doi.org/10.1016/S0167-2738(01)00677-4.
(19) Kim, S. Isn't the Space-Charge Potential in Ceria-Based Solid Electrolytes Largely Overestimated? *Phys. Chem. Chem. Phys.* **2016**, *18* (29), 19787–19791. https://doi.org/10.1039/C6CP02177H.
(20) Göbel, M. C.; Gregori, G.; Maier, J. Size Effects on the Electrical Conductivity of Ceria: Achieving Low Space Charge Potentials in Nanocrystalline Thin Films. *J. Phys. Chem. C* **2013**, *117* (44), 22560–22568. https://doi.org/10.1021/jp407585w.
(21) Newville, M. Fundamentals of XAFS. *Reviews in Mineralogy and Geochemistry* **2014**, *78* (1), 33–74. https://doi.org/10.2138/rmg.2014.78.2.
(22) Henderson, G. S.; de Groot, F. M. F.; Moulton, B. J. A. X-Ray Absorption Near-Edge Structure (XANES) Spectroscopy. *Reviews in Mineralogy and Geochemistry* **2014**, *78* (1), 75–138. https://doi.org/10.2138/rmg.2014.78.3.
(23) Binnig, G.; Quate, C. F.; Gerber, Ch. Atomic Force Microscope. *Phys. Rev. Lett.* **1986**, *56* (9), 930–933. https://doi.org/10.1103/PhysRevLett.56.930.
(24) Mizusaki, J.; Mima, Y.; Yamauchi, S.; Fueki, K.; Tagawa, H. Nonstoichiometry of the Perovskite-Type Oxides La1−xSrxCoO3−δ. *Journal of Solid State Chemistry* **1989**, *80* (1), 102–111. https://doi.org/10.1016/0022-4596(89)90036-4.
(25) Wilson, J. R.; Sase, M.; Kawada, T.; Adler, S. B. Measurement of Oxygen Exchange Kinetics on Thin-Film La0.6Sr0.4CoO3 − δ Using Nonlinear Electrochemical Impedance Spectroscopy. *Electrochem. Solid-State Lett.* **2007**, *10* (5), B81–B86. https://doi.org/10.1149/1.2710178.
(26) Kawada, T.; Suzuki, J.; Sase, M.; Kaimai, A.; Yashiro, K.; Nigara, Y.; Mizusaki, J.; Kawamura, K.; Yugami, H. Determination of Oxygen Vacancy Concentration in a Thin Film of La0.6Sr0.4CoO3 − δ by an Electrochemical Method. *J. Electrochem. Soc.* **2002**, *149* (7), E252–E259. https://doi.org/10.1149/1.1479728.
(27) Amezawa, K.; Orikasa, Y.; Ina, T.; Unemoto, A.; Sase, M.; Watanabe, H.; Fukutsuka, T.; Kawada, T.; Terada, Y.; Uchimoto, Y. Electronic and Local Structures of La1-x SrxCoO3-δ Studied by In-Situ Micro XAS Measurements. *ECS Trans.* **2008**, *13* (26), 161–164. https://doi.org/10.1149/1.3050388.
(28) Amezawa, K.; Fujimaki, Y.; Nakamura, T.; Bagarinao, K. D.-; Yamaji, K.; Nitta, K.; Terada, Y.; Iguchi, F.; Yashiro, K.; Yugami, H.; Kawada, T. (Invited) Determination of Effective Reaction Area in a Mixed-Conducting SOFC Cathode. *ECS Trans.* **2015**, *66* (2), 129–135. https://doi.org/10.1149/06602.0129ecst.
(29) Amezawa, K.; Fujimaki, Y.; Mizuno, K.; Kimura, Y.; Nakamura, T.; Nitta, K.; Terada, Y.; Iguchi, F.; Yugami, H.; Yashiro, K.; Kawada, T. (Invited) Triple Phase Boundary Reaction in a Mixed-Conducting SOFC Cathode. *ECS Trans.* **2017**, *77* (10), 41–47. https://doi.org/10.1149/07710.0041ecst.

(30) Orikasa, Y.; Ina, T.; Nakao, T.; Mineshige, A.; Amezawa, K.; Oishi, M.; Arai, H.; Ogumi, Z.; Uchimoto, Y. X-Ray Absorption Spectroscopic Study on La0.6Sr0.4CoO3−δ Cathode Materials Related with Oxygen Vacancy Formation. *J. Phys. Chem. C* **2011**, *115* (33), 16433–16438. https://doi.org/10.1021/jp2029642.

(31) Fujimaki, Y.; Watanabe, H.; Terada, Y.; Nakamura, T.; Yashiro, K.; Hashimoto, S.; Kawada, T.; Amezawa, K. Direct Evaluation of Oxygen Chemical Potential Distribution in an SOFC Cathode by In Situ X-Ray Absorption Spectroscopy. *ECS Trans.* **2013**, *57* (1), 1925–1932. https://doi.org/10.1149/05701.1925ecst.

(32) Adler, S. B. Chemical Expansivity of Electrochemical Ceramics. *Journal of the American Ceramic Society* **2001**, *84* (9), 2117–2119. https://doi.org/10.1111/j.1151-2916.2001.tb00968.x.

(33) Ohno, Y.; Nagata, S.; Sato, H. Properties of Oxides for High Temperature Solid Electrolyte Fuel Cell. *Solid State Ionics* **1983**, *9–10*, 1001–1007. https://doi.org/10.1016/0167-2738(83)90122-4.

(34) Boukamp, B. A.; Bouwmeester, H. J. M. Interpretation of the Gerischer Impedance in Solid State Ionics. *Solid State Ionics* **2003**, *157* (1), 29–33. https://doi.org/10.1016/S0167-2738(02)00185-6.

(35) Guay, D.; Tourillon, G.; Dartyge, E.; Fontaine, A.; Tolentino, H. In Situ Observations of Electrochemical Inclusion of Copper and Iron Species in a Conducting Organic Polymer by Using Time-Resolved X-Ray Absorption Spectroscopy. *J. Electrochem. Soc.* **1991**, *138* (2), 399. https://doi.org/10.1149/1.2085597.

(36) Lim, J.; Li, Y.; Alsem, D. H.; So, H.; Lee, S. C.; Bai, P.; Cogswell, D. A.; Liu, X.; Jin, N.; Yu, Y.; Salmon, N. J.; Shapiro, D. A.; Bazant, M. Z.; Tyliszczak, T.; Chueh, W. C. Origin and Hysteresis of Lithium Compositional Spatiodynamics within Battery Primary Particles. *Science* **2016**, *353* (6299), 566–571. https://doi.org/10.1126/science.aaf4914.

(37) Li, Y.; Weker, J. N.; Gent, W. E.; Mueller, D. N.; Lim, J.; Cogswell, D. A.; Tyliszczak, T.; Chueh, W. C. Dichotomy in the Lithiation Pathway of Ellipsoidal and Platelet LiFePO4 Particles Revealed through Nanoscale Operando State-of-Charge Imaging. *Advanced Functional Materials* **2015**, *25* (24), 3677–3687. https://doi.org/10.1002/adfm.201500286.

(38) Ishiguro, N.; Saida, T.; Uruga, T.; Nagamatsu, S.; Sekizawa, O.; Nitta, K.; Yamamoto, T.; Ohkoshi, S.; Iwasawa, Y.; Yokoyama, T.; Tada, M. Operando Time-Resolved X-Ray Absorption Fine Structure Study for Surface Events on a Pt3Co/C Cathode Catalyst in a Polymer Electrolyte Fuel Cell during Voltage-Operating Processes. *ACS Catal.* **2012**, *2* (7), 1319–1330. https://doi.org/10.1021/cs300228p.

(39) Ishiguro, N.; Kityakarn, S.; Sekizawa, O.; Uruga, T.; Sasabe, T.; Nagasawa, K.; Yokoyama, T.; Tada, M. Rate Enhancements in Structural Transformations of Pt–Co and Pt–Ni Bimetallic Cathode Catalysts in Polymer Electrolyte Fuel Cells Studied by in Situ Time-Resolved X-Ray Absorption Fine Structure. *J. Phys. Chem. C* **2014**, *118* (29), 15874–15883. https://doi.org/10.1021/jp504738p.

(40) Ishiguro, N.; Tada, M. Structural Kinetics of Cathode Events on Polymer Electrolyte Fuel Cell Catalysts Studied by Operando Time-Resolved XAFS. *Catal Lett* **2018**, *148* (6), 1597–1609. https://doi.org/10.1007/s10562-018-2383-7.

(41) Minguzzi, A.; Lugaresi, O.; Locatelli, C.; Rondinini, S.; D'Acapito, F.; Achilli, E.; Ghigna, P. Fixed Energy X-Ray Absorption Voltammetry. *Anal. Chem.* **2013**, *85* (15), 7009–7013. https://doi.org/10.1021/ac401414v.

(42) Lyons, R. G. Three. The Discrete Fourier Transform. In *Understanding Digital Signal Processing*; Pretince Hall PTR: Upper Saddle River, NJ, 2004.
(43) Fleig, J.; Baumann, F. S.; Brichzin, V.; Kim, H.-R.; Jamnik, J.; Cristiani, G.; Habermeier, H.-U.; Maier, J. Thin Film Microelectrodes in SOFC Electrode Research. *Fuel Cells* **2006**, *6* (3–4), 284–292. https://doi.org/10.1002/fuce.200500209.
(44) Chueh, W. C.; Haile, S. M. Electrochemistry of Mixed Oxygen Ion and Electron Conducting Electrodes in Solid Electrolyte Cells. *Annu. Rev. Chem. Biomol. Eng.* **2012**, *3* (1), 313–341. https://doi.org/10.1146/annurev-chembioeng-073009-101000.
(45) Siebenhofer, M.; Huber, T. M.; Friedbacher, G.; Artner, W.; Fleig, J.; Kubicek, M. Oxygen Exchange Kinetics and Nonstoichiometry of Pristine La0.6Sr0.4CoO3−δ Thin Films Unaltered by Degradation. *J. Mater. Chem. A* **2020**, *8* (16), 7968–7979. https://doi.org/10.1039/C9TA13020A.
(46) Orikasa, Y.; Ina, T.; Nakao, T.; Mineshige, A.; Amezawa, K.; Oishi, M.; Arai, H.; Ogumi, Z.; Uchimoto, Y. An X-Ray Absorption Spectroscopic Study on Mixed Conductive La0.6Sr0.4Co0.8Fe0.2O3−δ Cathodes. I. Electrical Conductivity and Electronic Structure. *Phys. Chem. Chem. Phys.* **2011**, *13* (37), 16637–16643. https://doi.org/10.1039/C1CP20982E.
(47) Abbate, M.; Fuggle, J. C.; Fujimori, A.; Tjeng, L. H.; Chen, C. T.; Potze, R.; Sawatzky, G. A.; Eisaki, H.; Uchida, S. Electronic Structure and Spin-State Transition of ${\mathrm{LaCoO}}_{3}$. *Phys. Rev. B* **1993**, *47* (24), 16124–16130. https://doi.org/10.1103/PhysRevB.47.16124.
(48) Wilson, J. R.; Schwartz, D. T.; Adler, S. B. Nonlinear Electrochemical Impedance Spectroscopy for Solid Oxide Fuel Cell Cathode Materials. *Electrochimica Acta* **2006**, *51* (8–9), 1389–1402. https://doi.org/10.1016/j.electacta.2005.02.109.
(49) Warburg, E. Polarization Capacity of Platinum. *Ann. Phys.* **1901**, *6*, 125.
(50) Adler, S. B.; Lane, J. A.; Steele, B. C. H. Electrode Kinetics of Porous Mixed-Conducting Oxygen Electrodes. *J. Electrochem. Soc.* **1996**, *143* (11), 3554–3564. https://doi.org/10.1149/1.1837252.
(51) Søgaard, M.; Hendriksen, P. V.; Mogensen, M.; Poulsen, F. W.; Skou, E. Oxygen Nonstoichiometry and Transport Properties of Strontium Substituted Lanthanum Cobaltite. *Solid State Ionics* **2006**, *177* (37), 3285–3296. https://doi.org/10.1016/j.ssi.2006.09.005.
(52) Huber, T. M.; Navickas, E.; Sasaki, K.; Yildiz, B.; Hutter, H.; Tuller, H.; Fleig, J. Interplay of Grain Size Dependent Electronic and Ionic Conductivity in Electrochemical Polarization Studies on Sr-Doped LaMnO3 (LSM) Thin Film Cathodes. *J. Electrochem. Soc.* **2018**, *165* (9), F702. https://doi.org/10.1149/2.1081809jes.
(53) Saranya, A. M.; Morata, A.; Pla, D.; Burriel, M.; Chiabrera, F.; Garbayo, I.; Hornés, A.; Kilner, J. A.; Tarancón, A. Unveiling the Outstanding Oxygen Mass Transport Properties of Mn-Rich Perovskites in Grain Boundary-Dominated La0.8Sr0.2(Mn1–XCox)0.85O3±δ Nanostructures. *Chem Mater* **2018**, *30* (16), 5621–5629. https://doi.org/10.1021/acs.chemmater.8b01771.
(54) Mutoro, E.; Crumlin, E. J.; Biegalski, M. D.; Christen, H. M.; Shao-Horn, Y. Enhanced Oxygen Reduction Activity on Surface-Decorated Perovskite Thin Films for Solid Oxide Fuel Cells. *Energy Environ. Sci.* **2011**, *4* (9), 3689–3696. https://doi.org/10.1039/C1EE01245B.

(55) Kubicek, M.; Limbeck, A.; Frömling, T.; Hutter, H.; Fleig, J. Relationship between Cation Segregation and the Electrochemical Oxygen Reduction Kinetics of La0.6Sr0.4CoO3−δ Thin Film Electrodes. *J. Electrochem. Soc.* **2011**, *158* (6), B727. https://doi.org/10.1149/1.3581114.

(56) Mizuno, Keita. Investigation of Reaction Pathways on Mixed Conducting Cathodes for Solid Oxide Fuel Cells by Using Model Electrodes. M.S, Tohoku University, Japan -- Sendai, 2018.

(57) Boukamp, B. A.; Verbraeken, M.; Blank, D. H. A.; Holtappels, P. SOFC-Anodes, Proof for a Finite-Length Type Gerischer Impedance? *Solid State Ionics* **2006**, *177* (26), 2539–2541. https://doi.org/10.1016/j.ssi.2006.03.002.

(58) Fu, Y.; Poizeau, S.; Bertei, A.; Qi, C.; Mohanram, A.; Pietras, J. D.; Bazant, M. Z. Heterogeneous Electrocatalysis in Porous Cathodes of Solid Oxide Fuel Cells. *Electrochimica Acta* **2015**, *159*, 71–80. https://doi.org/10.1016/j.electacta.2015.01.120.

(59) Boukamp, B. A.; Rolle, A. Analysis and Application of Distribution of Relaxation Times in Solid State Ionics. *Solid State Ionics* **2017**, *302*, 12–18. https://doi.org/10.1016/j.ssi.2016.10.009.

(60) Nielsen, J.; Jacobsen, T.; Wandel, M. Impedance of Porous IT-SOFC LSCF:CGO Composite Cathodes. *Electrochimica Acta* **2011**, *56* (23), 7963–7974. https://doi.org/10.1016/j.electacta.2011.05.042.

(61) Shin, E.-C.; Ma, J.; Ahn, P.-A.; Seo, H.-H.; Nguyen, D. T.; Lee, J. S. Deconvolution of Four Transmission-Line-Model Impedances in Ni-YSZ/YSZ/LSM Solid Oxide Cells and Mechanistic Insights. *Electrochimica Acta* **2016**, *188*, 240–253. https://doi.org/10.1016/j.electacta.2015.11.118.

(62) Boukamp, B. A.; Rolle, A. Use of a Distribution Function of Relaxation Times (DFRT) in Impedance Analysis of SOFC Electrodes. *Solid State Ionics* **2018**, *314*, 103–111. https://doi.org/10.1016/j.ssi.2017.11.021.

(63) Adler, S. B.; Chen, X. Y.; Wilson, J. R. Mechanisms and Rate Laws for Oxygen Exchange on Mixed-Conducting Oxide Surfaces. *Journal of Catalysis* **2007**, *245* (1), 91–109. https://doi.org/10.1016/j.jcat.2006.09.019.

(64) Lankhorst, M. H. R.; Bouwmeester, H. J. M.; Verweij, H. High-Temperature Coulometric Titration of La1−xSrxCoO3−δ: Evidence for the Effect of Electronic Band Structure on Nonstoichiometry Behavior. *Journal of Solid State Chemistry* **1997**, *133* (2), 555–567. https://doi.org/10.1006/jssc.1997.7531.

(65) Newman, J. S. *Electrochemical Systems*, Fourth edition.; Electrochemical Society series; John Wiley & Sons Inc: Hoboken, NJ, 2021.

(66) Tuller, H. L. Ionic Conduction in Nanocrystalline Materials. *Solid State Ionics* **2000**, *131* (1–2), 143–157. https://doi.org/10.1016/S0167-2738(00)00629-9.

(67) Kim, S.; Fleig, J.; Maier, J. Space Charge Conduction: Simple Analytical Solutions for Ionic and Mixed Conductors and Application to Nanocrystalline Ceria. *Phys. Chem. Chem. Phys.* **2003**, *5* (11), 2268–2273. https://doi.org/10.1039/B300170A.

(68) Jasper, A.; Kilner, J. A.; McComb, D. W. TEM and Impedance Spectroscopy of Doped Ceria Electrolytes. *Solid State Ionics* **2008**, *179* (21), 904–908. https://doi.org/10.1016/j.ssi.2008.02.001.

(69) Chiang, Y.-M.; Lavik, E. B.; Blom, D. A. Defect Thermodynamics and Electrical Properties of Nanocrystalline Oxides: Pure and Doped CeO2. *Nanostructured Materials* **1997**, *9* (1), 633–642. https://doi.org/10.1016/S0965-9773(97)00142-6.

(70) Wang, S.; Inaba, H.; Tagawa, H.; Dokiya, M.; Hashimoto, T. Nonstoichiometry of Ce0.9Gd0.1O1.95−x. *Solid State Ionics* **1998**, *107* (1–2), 73–79. https://doi.org/10.1016/S0167-2738(97)00519-5.
(71) Yashiro, K.; Onuma, S.; Kaimai, A.; Nigara, Y.; Kawada, T.; Mizusaki, J.; Kawamura, K.; Horita, T.; Yokokawa, H. Mass Transport Properties of Ce0.9Gd0.1O2−δ at the Surface and in the Bulk. *Solid State Ionics* **2002**, *152–153*, 469–476. https://doi.org/10.1016/S0167-2738(02)00375-2.
(72) Tuller, H. L.; Nowick, A. S. Defect Structure and Electrical Properties of Nonstoichiometric CeO2 Single Crystals. *J. Electrochem. Soc.* **1979**, *126* (2), 209–217. https://doi.org/10.1149/1.2129007.
(73) Guo, X.; Waser, R. Electrical Properties of the Grain Boundaries of Oxygen Ion Conductors: Acceptor-Doped Zirconia and Ceria. *Progress in Materials Science* **2006**, *51* (2), 151–210. https://doi.org/10.1016/j.pmatsci.2005.07.001.
(74) Li, J.; Li, J.-F.; Yu, Q.; Chen, Q. N.; Xie, S. Strain-Based Scanning Probe Microscopies for Functional Materials, Biological Structures, and Electrochemical Systems. *Journal of Materiomics* **2015**, *1* (1), 3–21. https://doi.org/10.1016/j.jmat.2015.03.001.
(75) Eshghinejad, A.; Esfahani, E. N.; Wang, P.; Xie, S.; Geary, T. C.; Adler, S. B.; Li, J. Scanning Thermo-Ionic Microscopy for Probing Local Electrochemistry at the Nanoscale. *Journal of Applied Physics* **2016**, *119* (20), 205110. https://doi.org/10.1063/1.4949473.
(76) Esfahani, E. N.; Eshghinejad, A.; Ou, Y.; Zhao, J.; Adler, S.; Li, J. Scanning Thermo-Ionic Microscopy: Probing Nanoscale Electrochemistry via Thermal Stress-Induced Oscillation. *Microscopy Today* **2017**, *25* (6), 12–19. https://doi.org/10.1017/S1551929517001043.
(77) Esfahani, E. N.; Liu, X.; Li, J. Imaging Ferroelectric Domains via Charge Gradient Microscopy Enhanced by Principal Component Analysis. *Journal of Materiomics* **2017**, *3* (4), 280–285. https://doi.org/10.1016/j.jmat.2017.07.001.
(78) Denton, A. R.; Ashcroft, N. W. Vegard's Law. *Phys. Rev. A* **1991**, *43* (6), 3161–3164. https://doi.org/10.1103/PhysRevA.43.3161.
(79) Funayama, K.; Nakamura, T.; Kuwata, N.; Kawamura, J.; Kawada, T.; Amezawa, K. Electromotive Force Measurements of LiCoO2 Electrode on a Lithium Ion-Conducting Glass Ceramics under Mechanical Stress. *Solid State Ionics* **2016**, *285*, 75–78. https://doi.org/10.1016/j.ssi.2015.09.009.
(80) Gonoi, Y.; Kimura, Y.; Yashiro, K.; Watanabe, S.; Hashimoto, S.; Kawada, T. Effect of Mechanical Stress on Oxygen Potential of Transition Metal Oxides. *J. Electrochem. Soc.* **2014**, *161* (11), F3111–F3116. https://doi.org/10.1149/2.0181411jes.
(81) Larché, F.; Cahn, J. W. A Linear Theory of Thermochemical Equilibrium of Solids under Stress. *Acta Metallurgica* **1973**, *21* (8), 1051–1063. https://doi.org/10.1016/0001-6160(73)90021-7.
(82) Jasper, A. J. TEM Studies of Interfaces in Fuel Cell Materials. **2010**.
(83) Bowman, W. J.; Kelly, M. N.; Rohrer, G. S.; Hernandez, C. A.; Crozier, P. A. Enhanced Ionic Conductivity in Electroceramics by Nanoscale Enrichment of Grain Boundaries with High Solute Concentration. *Nanoscale* **2017**, *9* (44), 17293–17302. https://doi.org/10.1039/C7NR06941C.
(84) Lin, Y.; Fang, S.; Su, D.; Brinkman, K. S.; Chen, F. Enhancing Grain Boundary Ionic Conductivity in Mixed Ionic–Electronic Conductors. *Nature Communications* **2015**, *6*, 6824. https://doi.org/10.1038/ncomms7824.